Results in Physics 18 (2020) 103179

Contents lists available at ScienceDirect

Results in Physics

journal homepage: www.elsevier.com/locate/rinp

Elastic scattering of electrons and positrons from ^{115}In atoms over the energy range 1 eV–0.5 GeV

Sanjida Afroz[a], M.M. Haque[a], A.K. Fazlul Haque[a], D.H. Jakubassa-Amundsen[b], M.Atiqur R. Patoary[a], M. Shorifuddoza[a], Mahmudul H. Khandker[a], M. Alfaz Uddin[c]

[a] Atomic Physics Lab, Department of Physics, University of Rajshahi, Rajshahi 6205, Bangladesh
[b] Mathematics Institute, University of Munich, 80333 Munich, Germany
[c] Department of Physics, Pabna University of Science and Technology, Bangladesh

ARTICLE INFO

Keywords:
Elastic electron and positron scattering
Spin asymmetry
Critical minima
Magnetic scattering

ABSTRACT

We present a theoretical study on the calculations of various cross sections related to the scattering of electrons and positrons from indium atoms. Our calculations cover the energy range 1 eV $\leqslant E_i \leqslant$ 0.5 GeV. We have employed two approaches, applicable for two domains of energy, based on the Dirac partial-wave analysis. In one approach, we have used both the atomic and nuclear potentials to calculate the cross sections for the low and intermediate energies. The other approach, valid for the high-energy scattering, utilizes only the nuclear potential for the phase-shift analysis, and considers the magnetic scattering from the nucleus too. We report the calculations of differential, integral, momentum-transfer and viscosity cross sections along with the spin asymmetries for the elastic scattering of electrons and positrons. Moreover, we have analyzed the critical minima in the elastic differential cross sections, and also computed the absorption and total cross sections. Our results agree reasonably with the available experimental data and other calculations.

1. Introduction

Results from the scattering theory in conjunction with the experimental investigations provide much knowledge about interactions between elementary particles composing the universe and the structure of bulk matter. Moreover, elastic scattering data are needed in many areas of science, industries and technologies. In particular, a fairly accurate estimate of the elastic scattering by electron (e^-) and positron (e^+) impact on various species in a wide energy range is in great demand for applications in the fields of chemical, biological, plasma and laser physics, and even astrophysics [1,2]. The elastic differential (DCS), integral (ICS), momentum-transfer (MTCS), viscosity (VCS), inelastic (INCS) and total (elastic + inelastic) (TCS) cross sections are important characteristics of the $e^{\pm}$-atom collisions. The comparative study of e^- and e^+ scattering helps in understanding and refining the collision dynamics.

The elastic DCS furnishes detailed informations on $e^{\pm}$-atom collision dynamics and on the optical potential. The Sherman function S, an additional degree of freedom, provides more detailed information on the collision process. Moreover, the measurements of the additional spin asymmetry parameters T and U [3] from beam electrons spin-polarized in the scattering plane allow for more complete insights into the atomic and nuclear structure [4]. The occurrence of the spin asymmetry parameter S is also predicted to serve as a signature for parity-violating electron-nucleus scattering [4]. If spin polarization of the target is not considered, the elastic DCS together with S, T and U provide a complete description of the elementary scattering process. The investigation of minima and the determination of critical minima (CM) points in the DCS is useful as, in the vicinity of the CMs, a complete spin polarization of the scattered projectile occurs [3,5]. Moreover, the studies of the CMs in DCS provide a crucial test of both the experimental results and collision dynamics.

So far, numerous attempts [3–22] have been made to formulate quantum mechanical approaches for solving lepton impact scattering problems of neutral atoms, ions and molecules. These are broadly classified into perturbation methods based on single-particle approximations like the Born theory, and non-perturbative techniques based on the multi-electron close-coupling approach [13,19,22]. Two perturbative methods that have been developed are the first-order distorted wave Born approximation (DWBA) [4,20] and the optical potential model (OPM) [3,5,7,8,14,15]. Both methods are capable of providing reliable scattering cross section data and require minimal computational resources. However, there are some advantages of one method over the other. While in the OPM only a spherical potential is

E-mail address: mhpdru@gmail.com (M.M. Haque).

https://doi.org/10.1016/j.rinp.2020.103179
Received 10 March 2020; Received in revised form 16 May 2020; Accepted 18 May 2020
Available online 07 June 2020
2211-3797/ © 2020 The Authors. Published by Elsevier B.V. This is an open access article under the CC BY license (http://creativecommons.org/licenses/by/4.0/).

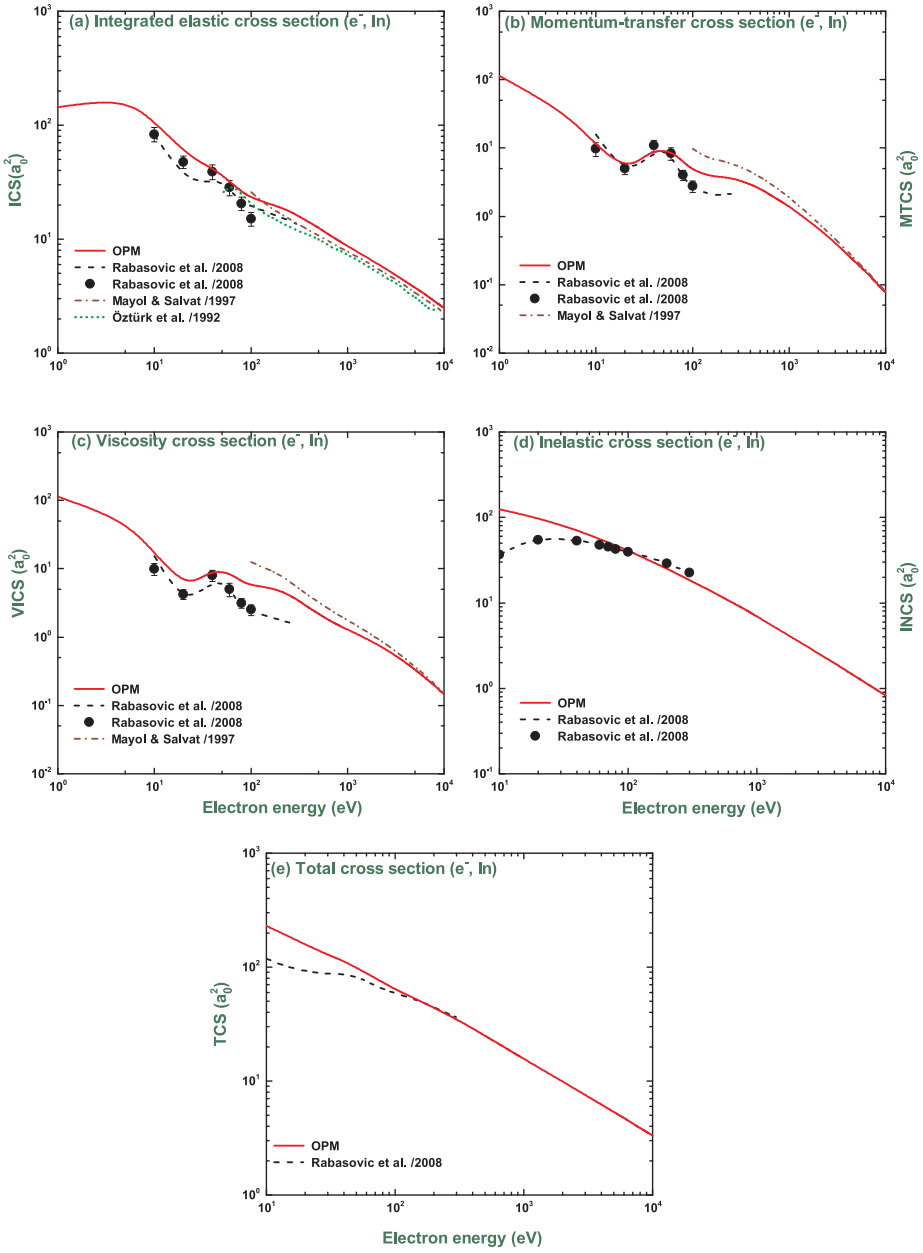

Fig. 1. Energy dependence of the (a) ICS, (b) MTCS, (c) VCS, (d) INCS and (e) TCS for electron-indium scattering. Theoretical: — line, present calculations using OPM; – – – line, Ref. [31]; ····· line, Ref. [35]; – ·–· line, Ref. [38]. Experimental: (•), Ref. [31].

considered, the DWBA allows for the inclusion of higher multipole components of the interaction [23]. On the other hand, for a given effective potential, the OPM method is valid to infinite order while the DWBA method is only accurate to first order perturbation theory. As for the incident energy, the OPM is successful in low to intermediate energy ($E_i \leqslant 1$ MeV) scattering where screening effects play a dominant role, while the DWBA is generally used for much higher energies where nuclear effects come into play.

The aim of the present investigation is to bridge the gap between the atomic physics and the nuclear physics regime, and to provide a comprehensive study which includes the nuclear magnetic effects on scattering. Encouraged by the reasonable success of our previous works [24–27], the present article studies all the features of $e^{\pm}$-In scattering over the energy domain 1 eV $\leqslant E_i \leqslant$ 0.5 GeV. This is achieved by using two theoretical approaches both of which are based on the phase-shift analysis which employs the partial-wave decomposition of the leptonic scattering states within the Dirac relativistic framework. The OPM approach is applied in the atomic regime and the nuclear structure approach (NSA), for the nuclear regime. In the NSA, for $E_i \gtrsim 50$ MeV, the phase shift analysis is supplemented with the Born approximation for magnetic scattering [4]. It is worth mentioning that most of our previous works [24–26], covering the all-out features up to GeV order, have not considered magnetic scattering as they have dealt with the targets (^{20}Ne, ^{174}Yb and ^{40}Ar) with zero spin. Although the investigations of Ref. [27] have included magnetic effects for the target ^{23}Na, they have not provided the analysis of the CM. In this paper, we have meticulously analyzed the CM points and the Sherman function in the vicinity of those CMs. Also is considered the magnetic scattering for the abundantly available ^{115}In isotope, because of its nuclear spin 9/2.

Indium, a metal with a low melting point, finds applications in astrophysics [28], plasma physics [29], semiconductor and optoelectronics [30], etc. However, experimental and theoretical studies on electrons and positrons scattered elastically from In have been fragmentary so far. Elastic DCS, TCS and spin asymmetry measurements for

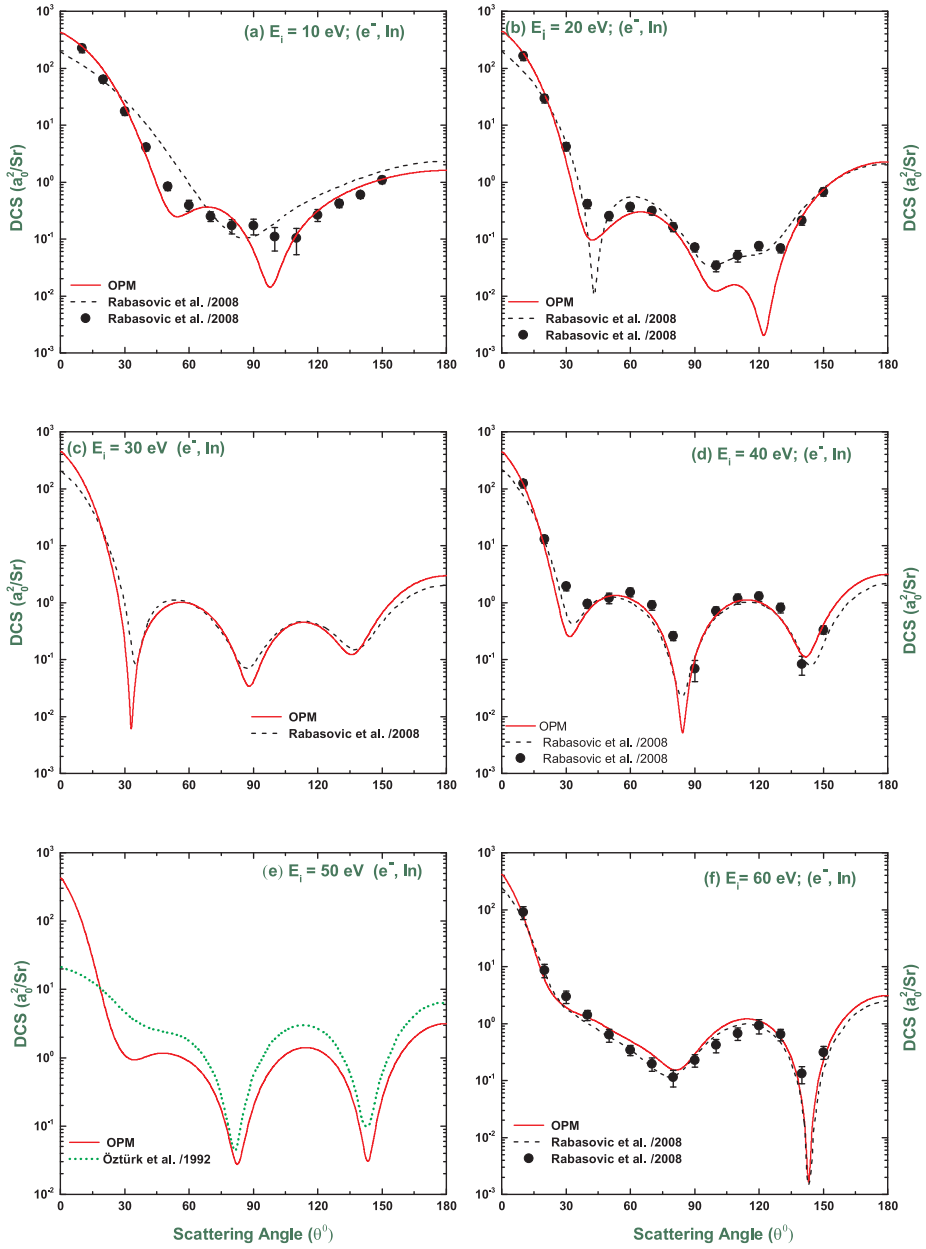

Fig. 2. Anglular distribution of the DCS for elastic scattering of 10, 20, 30, 40, 50 and 60 eV electrons from indium in units of a_o^2/Sr: — line, present calculations using OPM; – – – line, Ref. [31]; ····· line, Ref. [35]; (•), experimental data of Ref. [31].

e^--In scattering were reported by four experimental groups [31–34]. As far as theoretical studies are concerned, we are aware of calculations for elastic DCS and TCS by Öztürk et al. [35], Rabasović et al. [31] (both using the OMP method) and Dapor and Miotello [36] (by using a central electrostatic field); spin-asymmetry S by Bostock et al. [22] and Bartschat [37] (both using the close-coupling approach). All these theoretical investigations are concerned with low to intermediate energy scattering (atomic physics regime), where nuclear effects are absent. For ultrarelativistic beam energies (the nuclear physics regime), theoretical calculations of TCS and transport cross sections were only reported by Mayol and Salvat [38]. However, these authors did not consider magnetic scattering. Not a single article, available in literature, studied the CM points and the Sherman function for lepton-In scattering system.

The materials of the paper are arranged as follows. In Section 2, the outline of the theory is presented. Section 3 provides the discussion and comparison of the results. Section 4 contains the conclusions. Atomic units are used throughout unless otherwise specified.

2. Theoretical models

2.1. Relativistic Dirac equation

The motion of a projectile of rest mass m_o traveling with velocity v in a central field $V(r)$ can be described by the relativistic Dirac equation as

$$[c\boldsymbol{\alpha}\cdot\mathbf{p} + \beta m_o c^2 + V(r)]\psi(\mathbf{r}) = E\psi(\mathbf{r}), \tag{1}$$

where E is the total energy expressed as $E = m_o\gamma c^2 = E_i + m_o c^2$ with m_o being the rest mass of the projectile, $\gamma = (1 - v^2/c^2)^{-1/2}$ and c, being the velocity of light in vacuum. Here, E_i, $\boldsymbol{\alpha}$ and β represent, respectively, the kinetic energy of the incident particle and the usual 4×4 Dirac matrices. The relativistic wave function $\psi(\mathbf{r})$ is a four-component spinor with quantum numbers κ, m. The function describes the scattering state

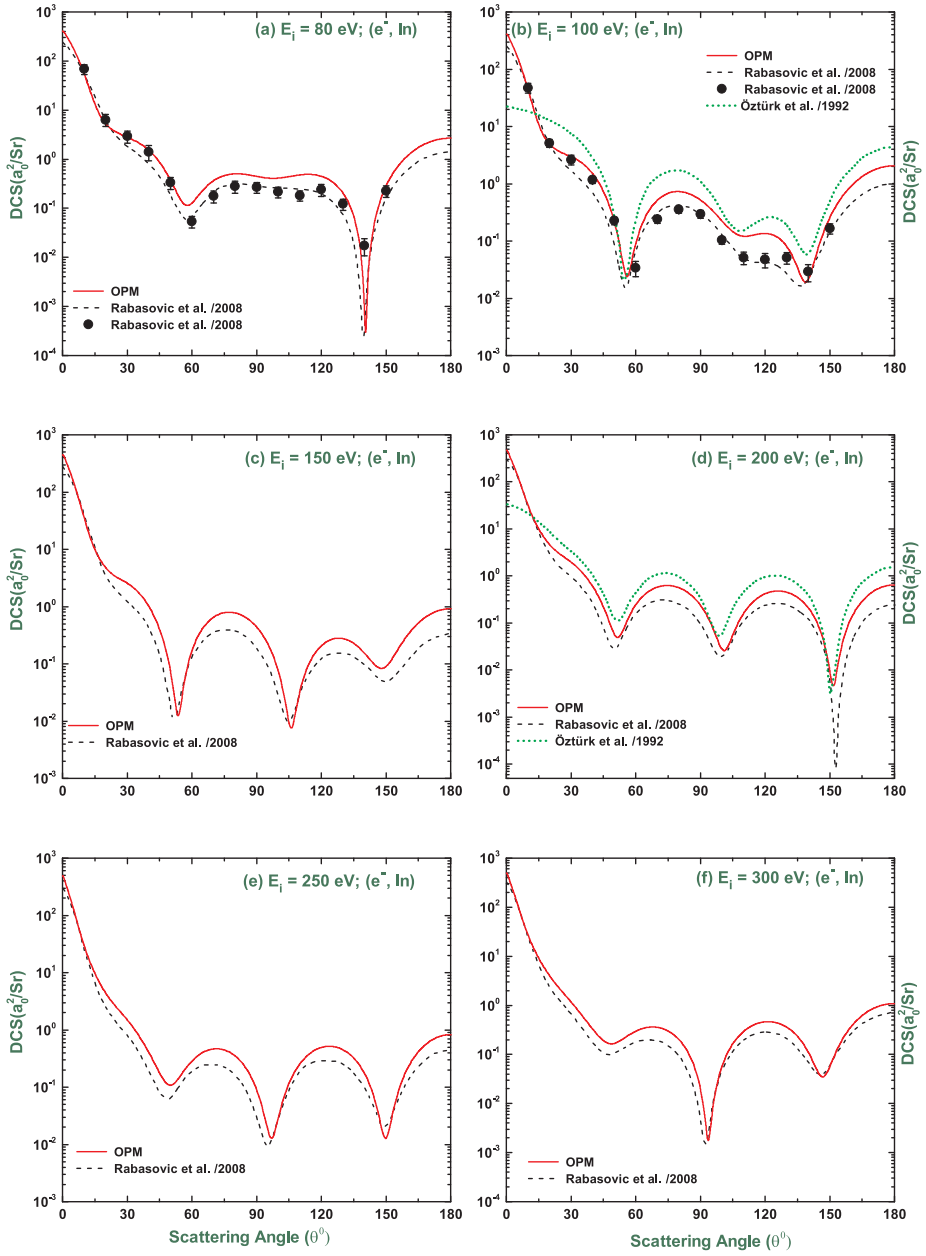

Fig. 3. Same as Fig. 2, but at impact energies of 80, 100, 150, 200, 250 and 300 eV.

of the projectile and is given by

$$\psi_{Ekm}(\vec{r}) = \frac{1}{r}\begin{pmatrix} P_{E\kappa}(r)\Omega_{\kappa,m}(\hat{r}) \\ iQ_{E\kappa}(r)\Omega_{-\kappa,m}(\hat{r}) \end{pmatrix}. \tag{2}$$

Here, $P_{E\kappa}(r)$ and $Q_{E\kappa}(r)$ are the large and small components of the radial part of the scattering wave function. $\Omega_{\kappa,m}(\hat{r})$ are the spherical harmonic spinors. κ is the relativistic quantum number defined in terms of the total angular momentum quantum number j and orbital angular momentum quantum number l as $\kappa = (l-j)(2j+1)$.

The functions $P_{E\kappa}(r)$ and $Q_{E\kappa}(r)$ satisfy the following set of coupled differential equations:

$$\frac{dP_{E\kappa}}{dr} = -\frac{\kappa}{r}P_{E\kappa}(r) + \frac{E_i - V + 2m_\circ c^2}{c}Q_{E\kappa}(r) \tag{3}$$

and

$$\frac{dQ_{E\kappa}}{dr} = -\frac{E_i - V}{c}P_{E\kappa}(r) + \frac{\kappa}{r}Q_{E\kappa}(r). \tag{4}$$

The scattering information is determined from the asymptotic form of the large component $P_{E\kappa}(r)$ of the scattering wave function, which can be expressed in terms of the complex phase shift δ_κ as

$$P_{E\kappa}(r) \simeq \sin\left(kr - l\frac{\pi}{2} + \delta_\kappa\right), \tag{5}$$

where k is the relativistic wave number of the projectile that is related to the momentum p and the kinetic energy E_i by

$$\hbar k = p, \quad (c\hbar k)^2 = E_i(E_i + 2m_\circ c^2). \tag{6}$$

The Eqs. (3) and (4) satisfying the asymptotic condition (5) are solved numerically using the subroutine package RADIAL [39].

2.2. The OPM method

In the OPM, the elastic scattering of a projectile from the target is formulated in terms of a local complex optical potential approximated from a non-local optical potential. This procedure is adapted for an easy

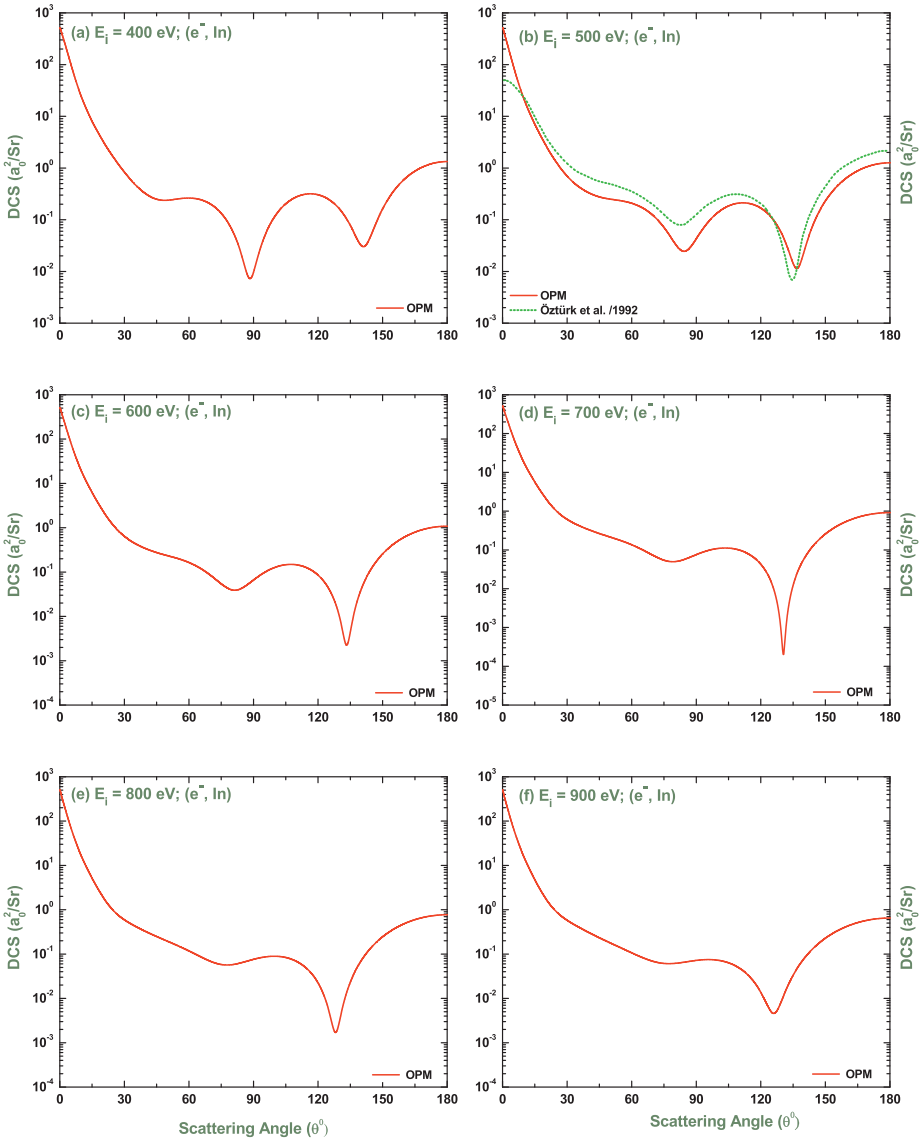

Fig. 4. Same as Fig. 2, but at impact energies of 400, 500, 600, 700, 800 and 900 eV.

implementation of the scattering problems. For low and intermediate energies ($E_i \leqslant 5$ MeV), the present study uses a complex optical potential to describe the effective interaction of electrons with the atomic target ^{115}In, which is given by

$$V(r) = V_{st}(r) + V_{ex}(r) + V_{cp}(r) - iW_{abs}(r), \tag{7}$$

where the real contributions $V_{st}(r)$, $V_{ex}(r)$ and $V_{cp}(r)$ are, respectively, the static, the exchange and the correlation-polarization potentials. W_{abs} represents the modulus of the imaginary absorption potential.

The projectile-atom electrostatic potential V_{st} is given by [40]

$$V_{st}(r) = Z_0\varphi(r), \tag{8}$$

where Z_0 is the charge of the projectile ($Z_0 = -1$ for electrons and $Z_0 = 1$ for positrons). The quantity $\varphi(r)$ is the sum of the nuclear interaction $\varphi_n(r)$ and the electronic interaction $\varphi_e(r)$. These two interactions can be expressed as

$$\varphi_n(r) = \left(\frac{1}{r}\int_0^r \rho_n(r')4\pi r'^2 dr' + \int_r^\infty \rho_n(r')4\pi r' dr'\right) \tag{9}$$

and

$$\varphi_e(r) = -\left(\frac{1}{r}\int_0^r \rho_e(r')4\pi r'^2 dr' + \int_r^\infty \rho_e(r')4\pi r' dr'\right), \tag{10}$$

where ρ_n and ρ_e are, respectively, the nuclear and electronic charge densities. In this study the electron density $\rho_e(r)$, represented by an analytical function $F(r)$, has been calculated from the numerical Hartree–Fock (HF) wave functions of Koga [41]. For a neutral atom, it satisfies the following normalization condition,

$$\int_0^\infty \rho_e(r)4\pi r^2 dr = Z, \tag{11}$$

with Z being the nuclear charge number of the target. For the charge density of the nucleus a Fermi nuclear charge distribution [34,40] is used (see Section 2.3).

The exchange potential $V_{ex}(r)$ in Eq. (7) for e^--In scattering is of semi-classical type, taken from Furness and McCarthy [42]. It is derived directly from the formal expression of the non-local exchange interaction with the help of a WKB-like approximation for the wave functions. It is expressed as

$$V_{ex}(r) = \frac{1}{2}[E_i - V_{st}(r)] - \frac{1}{2}\{[E_i - V_{st}(r)]^2 + 4\pi\rho_e(r)\}^{1/2}. \tag{12}$$

For the calculation of cross sections for positron scattering, the same type of optical potential as in (7) is used, excluding the exchange part $V_{ex}(r)$ as there is no exchange between incident positron and bound electrons.

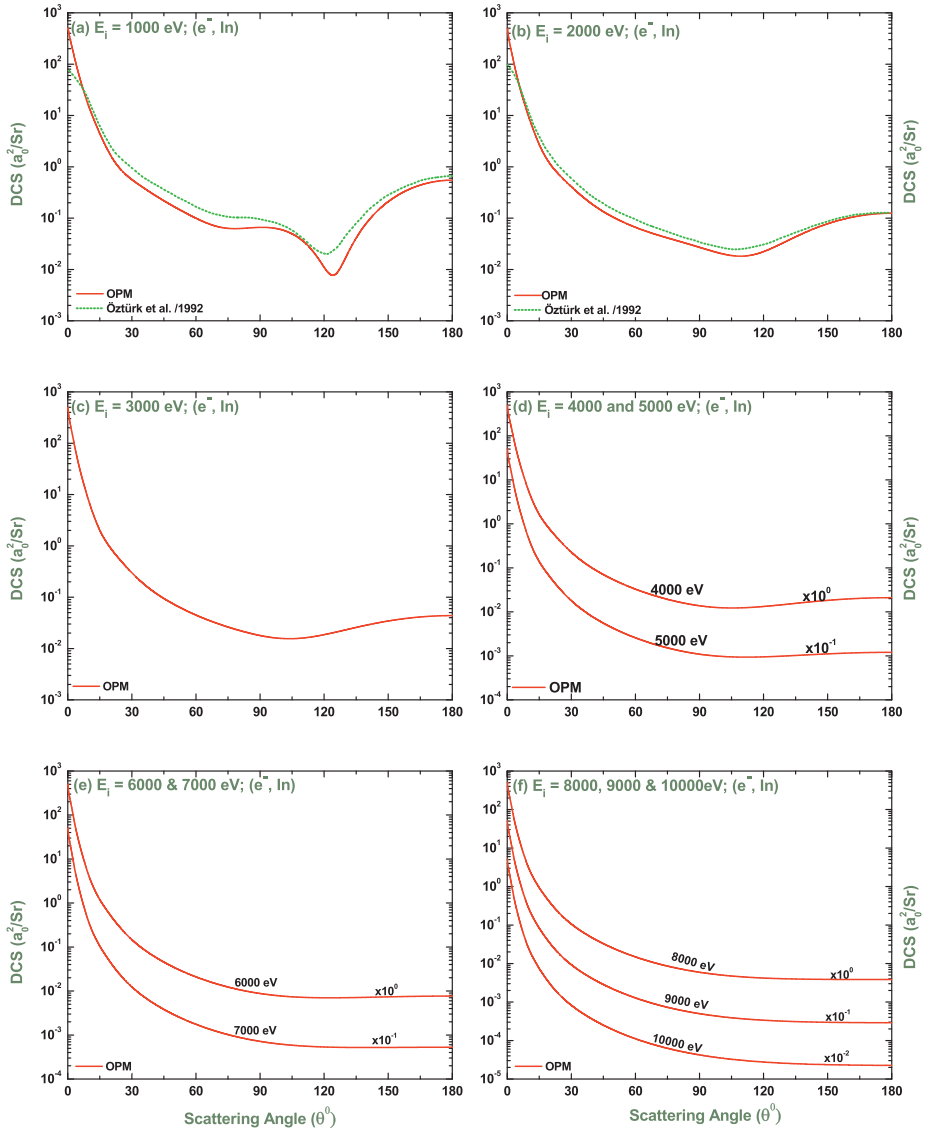

Fig. 5. Same as Fig. 2, but at impact energies of 1000, 2000, 3000, 4000, 5000, 6000, 7000, 8000, 9000 and 10000 eV.

Table 1
The positions of the DCS CM for the elastic e^--In scattering using our OPM. Also are presented those obtained by Rabasović et al. [31]. SEPS$_o$ and SEPAS$_o$ are the approaches without and with absorption respectively.

Present calculation				Rabasović et al. [31]			
OPM				SEPS$_o$		SEPAS$_o$	
E_c (eV)	θ_c (deg.)	$\lvert A(\theta)\rvert^2$ (a_0^2/Sr)	$\lvert B(\theta)\rvert^2$ (a_0^2/Sr)	E_c (eV)	θ_c (deg.)	E_c (eV)	θ_c (deg.)
6.802	105.4	3.24E−03	8.28E−03	–	–	–	–
14.782	50.6	1.19E−05	3.36E−03	–	–	–	–
17.68	106.6	3.29E−05	2.04E−03	–	–	–	–
19.32	120.2	9.58E−06	1.18E−03	18.5	114.98	–	–
31.32	32.6	7.34E−05	1.29E−03	–	–	–	–
42.75	83.8	3.83E−05	1.62E−03	42.7	84.18	46.3	81.84
64.842	142.6	1.13E−07	1.19E−04	60.4	142.5	56.6	143.16
67.45	142.2	1.35E−04	1.36E−04	–	–	–	–
79.46	140.6	8.56E−08	1.89E−04	75.5	140.33	81.5	138.37
133.93	107.8	2.29E−06	3.99E−04	131.9	106.95	126.2	108.13
215.41	151.4	1.51E−07	6.14E−05	205.7	151.82	201.4	152.88
325.5	92.2	2.64E−06	3.18E−04	300.9	93.13	330	91.01
695.47	130.6	4.14E−07	1.69E−04	–	–	–	–

The correlation-polarization potential in Eq. (7) stems from the polarization of the target electron cloud by the incident projectiles. The present study employs the global polarization potential V_{cp}, which is a combination of the parameter-free long-range polarization potential V_{cps} and a local-density approximation (LDA) to the correlation potential, V_{co}. This correlation-polarization potential can be expressed as

$$V_{cp}(r) \equiv \begin{cases} \max\{V_{co}(r),\, V_{cps}(r)\} & \text{if} \quad r \leqslant r_c \\ V_{cps}(r) & \text{if} \quad r > r_c. \end{cases} \tag{13}$$

The two contributions to the polarization potential, $V_{co}(r)$ and $V_{cps}(r)$, intersect for the first time at r_c. At large distances ($r > r_c$), the polarization potential has the well-known asymptotic form,

$$V_{cps}(r) = -\frac{\alpha}{2(r^2 + d^2)^2}, \tag{14}$$

where α is the static dipole polarizability of the target atom. The constant d is obtained from the equation

$$V_{cps}(0) = -\alpha/2d^4 \approx V_{co}(0). \tag{15}$$

Thus

$$d = (-\alpha/2V_{co}(0))^{1/4}. \tag{16}$$

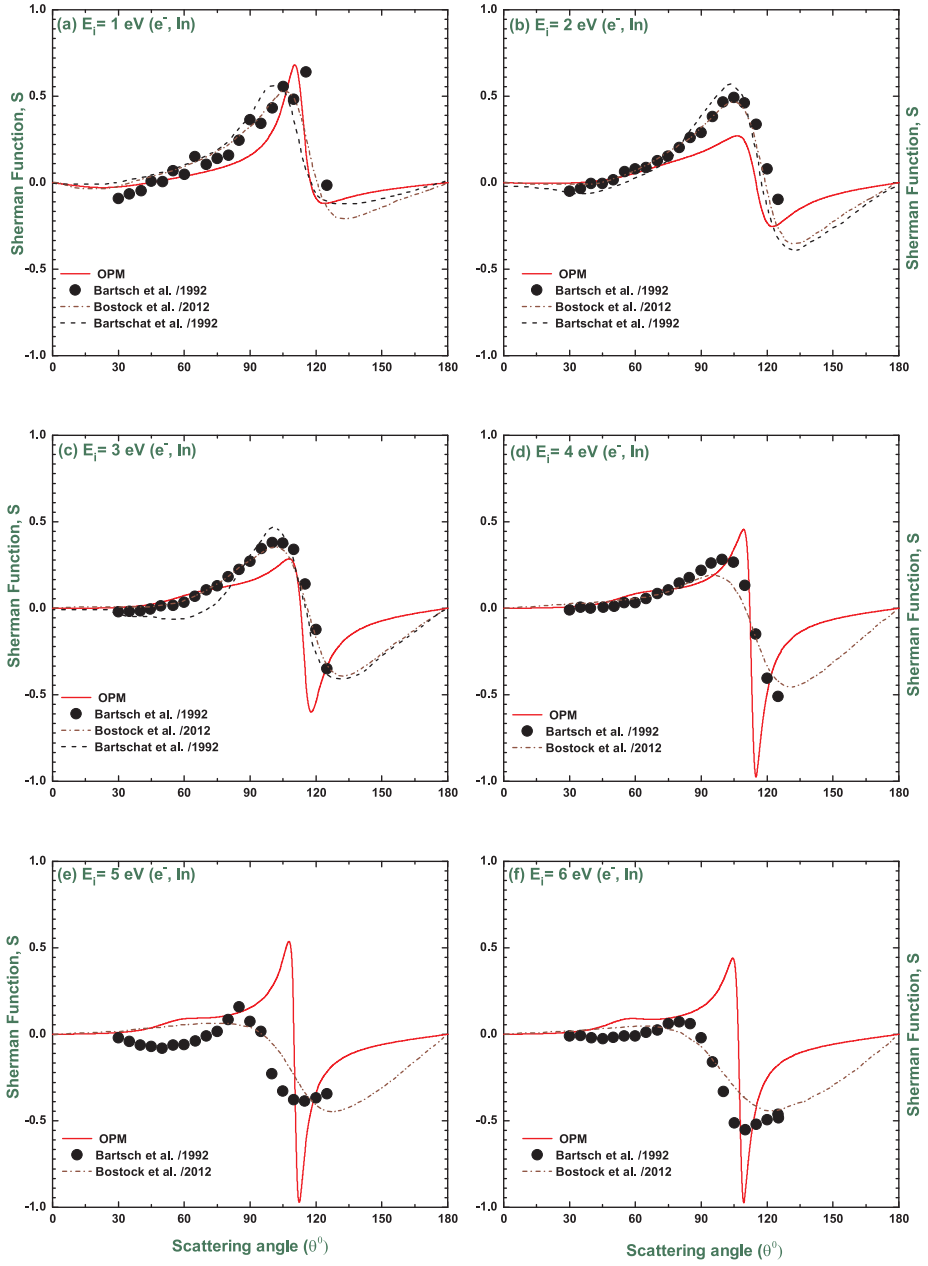

Fig. 6. The Sherman function S for elastic scattering of 1, 2, 3, 4, 5 and 6 eV electrons from indium: — curves, present calculations (OPM); – · – · – curves, Ref. [22]; – – – curves, Ref. [37]; (•), experimental data of Ref. [32].

In LDA, the local atomic electron density $\rho(r)$ is treated as a free electron gas (FEG) and the correlation energy of the projectile at r is calculated on the basis of its interaction with this FEG. This correlation energy is calculated as the functional derivative of the FEG correlation energy with respect to $\rho_e(r)$. The density parameter is defined as

$$r_s \equiv \left[\frac{3}{4\pi\rho_e(r)}\right]^{\frac{1}{3}}. \tag{17}$$

In the ELSEPA code [40], for electron scattering, the parameterization is employed as

$$V_{co}(r) = [0.0311\ln(r_s) - 0.0584 + 0.00133r_s\ln(r_s) - 0.0084r_s] \tag{18}$$

for $r_s < 1$, and

$$V_{co}(r) = \beta_o \frac{1 + (7/6)\beta_1 r_s^{\frac{1}{2}} + (4/3)\beta_2 r_s}{(1 + \beta_1 r_s^{\frac{1}{2}} + \beta_2 r_s)^2} \tag{19}$$

for $r_s \geqslant 1$, where $\beta_0 = -0.1423$, $\beta_1 = 1.0529$ and $\beta_2 = 0.3334$.

For positron impact scattering, we use the correlation polarization potential of Jain [43] as given by

$$V_{co}^{(+)}(r) = \frac{1}{2}[-1.82r_s^{-1/2} + [0.051\ln(r_s) - 0.115]\ln(r_s) + 1.167] \tag{20}$$

for $r_s < 0.302$,

$$V_{co}^{(+)}(r) = \frac{1}{2}[-0.92305 - 0.09098r_s^{-2}] \tag{21}$$

for $0.302 \leqslant r_s < 0.56$, and

$$V_{co}^{(+)}(r) = \frac{1}{2}\left[-\frac{8.7674r_s}{(r_s+2.5)^3} + \frac{-13.151 + 0.9552r_s}{(r_s+2.5)^2} + \frac{2.8655}{(r_s+2.5)} - 0.6298\right]$$

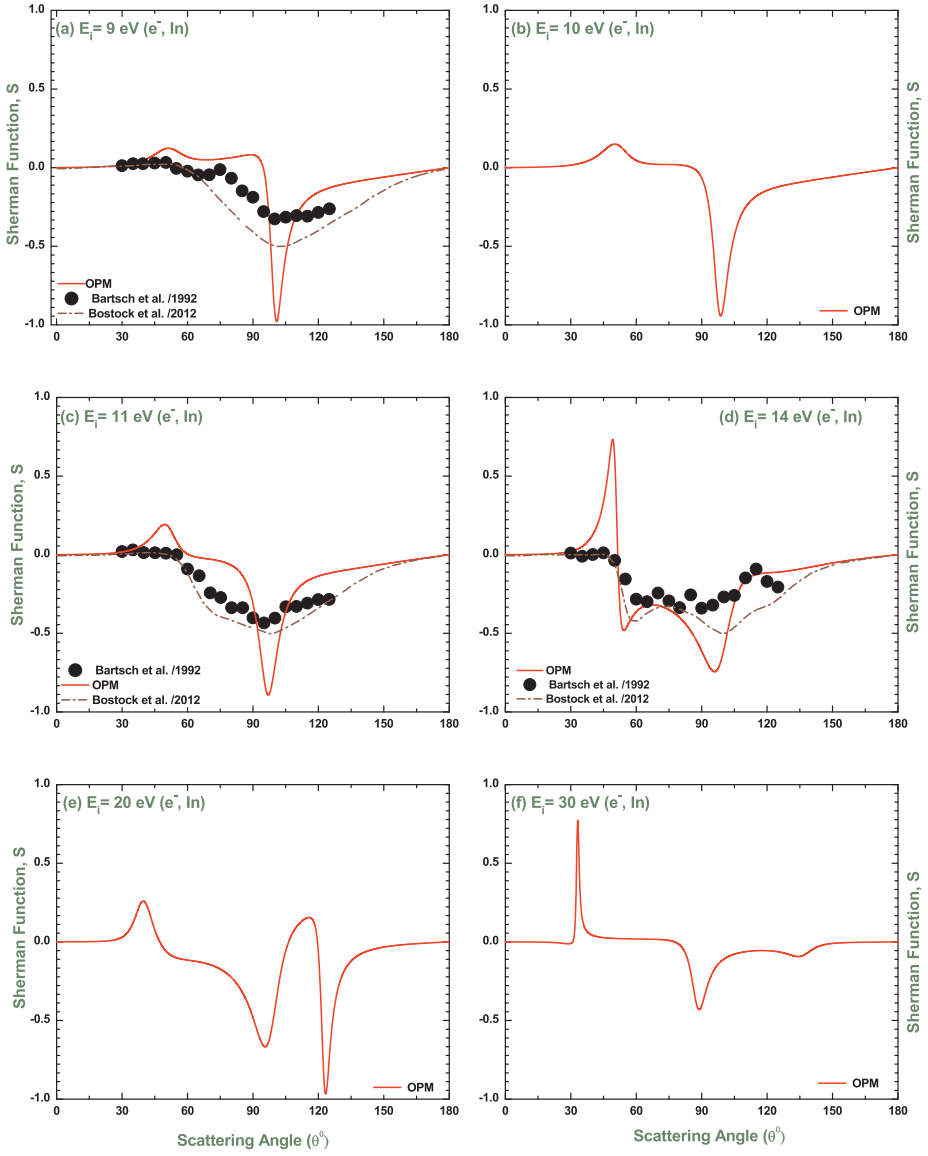

Fig. 7. Same as Fig. 6, but at impact energies of 9, 10, 11, 14, 20 and 30 eV.

for $0.56 \leqslant r_s < 8.0$.

As the asymptotic region $r_s \geqslant 8$ is the range beyond the crossing point, the polarization potential is accurately given by Eq. (14).

The imaginary component $W_{abs}(r)$ in Eq. (7) accounts for the loss of incident flux to various inelastic channels during the collision. This absorption potential depends on the cross section for binary collisions between the projectile and target electron. Such collisions excite the target electron to a higher energy state and contribute to the depletion of the elastic channel. For electron scattering, the relativistic corrected $W_{abs}(r)$, as proposed by Salvat et al. [40], is given by

$$W_{abs}(r) = \sqrt{\frac{2(E_L + m_o c^2)^2}{m_o c^2 (E_L + 2m_o c^2)}} \times A_{abs} \frac{1}{2} [v_L \rho_e(r) \sigma_{bc}(E_L, \rho, \Delta)], \tag{22}$$

where v_L is the velocity with which the projectile interacts as if it were moving within a homogeneous gas of density ρ_e. This projectile velocity is given by $v_L = (2E_L/m_o)^{1/2}$ corresponding to the local kinetic energy $E_L(r) = E_i - V_{st}(r) - V_{ex}(r)$. $\sigma_{bc}(E_L, \rho, \Delta)$ is the cross section for the binary collision of the electron with the degenerate FEG [42] involving energy transfers greater than a certain energy gap Δ. In the present electron-indium scattering, the value of the empirical parameter A_{abs}, resulting from a best fit to experiment, has been chosen as 2.8 for the calculations of the various cross sections. For positron scattering, the same expression (22) for $W_{abs}(r)$ has been used with $A_{abs} = 1.5$.

The energy gap Δ is the threshold energy for the inelastic channel and accounts for the minimum energy lost by the projectile. For the present computation, the energy gap Δ is adopted as

$$\Delta = \begin{cases} \epsilon_1 & \text{for electrons,} \\ \max\{I - 6.8 \text{ eV}, 0\} & \text{for positrons.} \end{cases} \tag{23}$$

Here $\epsilon_1 = 0.274$ eV [44] and $I = 5.7864$ eV [45] are, respectively, the first excitation energy and the ionization potential of the target atom. The quantity 6.8 eV is the ground-state binding energy of the positronium atom. Since $I < 6.8$ eV, positronium formation is possible at arbitrary energy.

The scattering of electrons and positrons by the complex optical potential $V(r)$ is completely described by the non-flip part A and the spin-flip part B of the elastic scattering amplitude f_e [5],

$$A = \frac{1}{2ik} \sum_{l=0}^{\infty} [(l+1)(e^{2i\delta_{-l-1}} - 1) + l(e^{2i\delta_l} - 1)] P_l(\cos\theta) \tag{24}$$

and

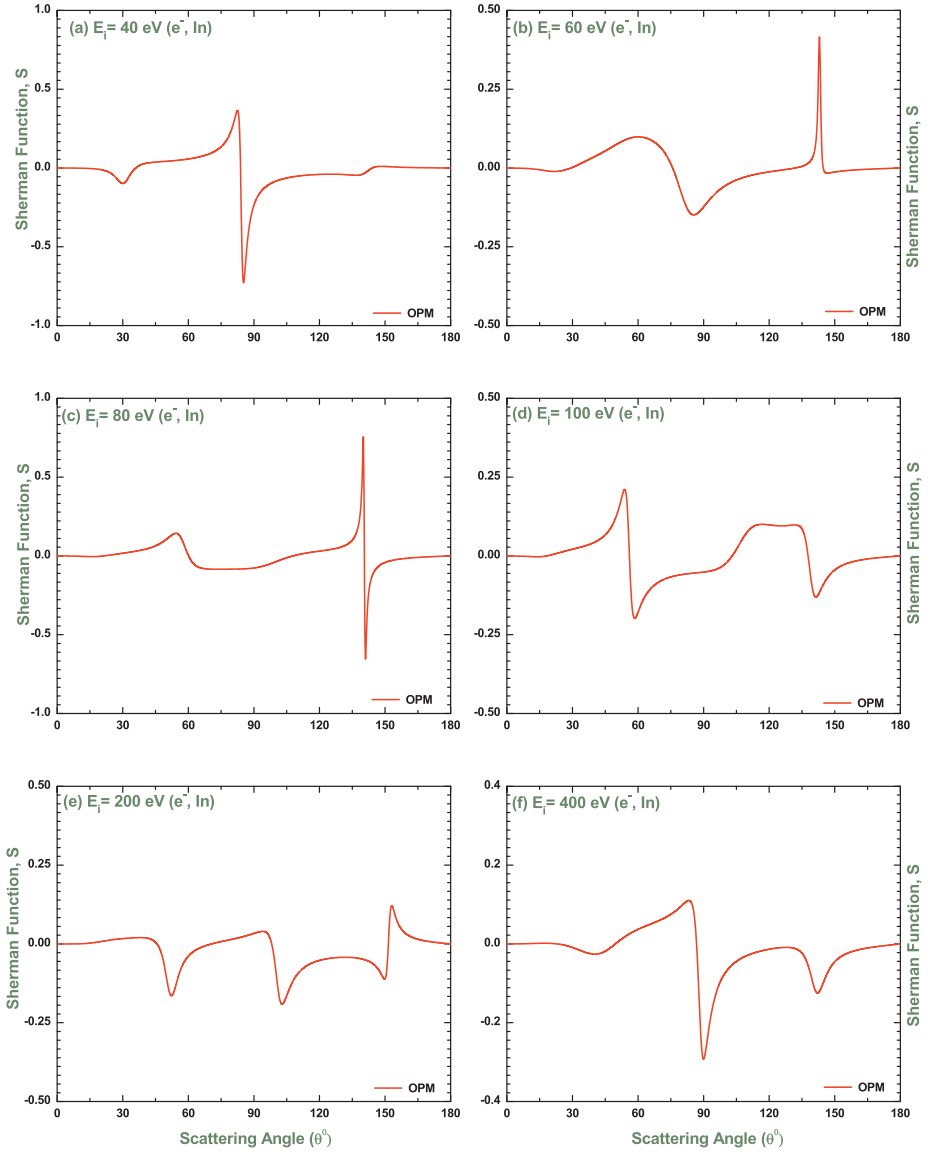

Fig. 8. Same as Fig. 6, but at impact energies of 40, 60, 80, 100, 200 and 400 eV.

$$B = -\frac{1}{2k}\sum_{l=1}^{\infty}(e^{2i\delta_l} - e^{2i\delta_{-l-1}})P_l^1(\cos\theta), \tag{25}$$

where $P_l(\cos\theta)$ and $P_l^1(\cos\theta)$ denote, respectively, the Legendre polynomials and associated Legendre functions. And θ is the scattering angle.

Once the phase shifts and the scattering amplitudes are determined, the elastic DCS for initially unpolarized electrons or positrons is obtained from the expression

$$\left(\frac{d\sigma}{d\Omega}\right)_0 = |A|^2 + |B|^2 \tag{26}$$

The integral, momentum-transfer, viscosity and total cross sections are, respectively, defined [5] as

$$\sigma_{el} = \int \frac{d\sigma}{d\Omega}d\Omega = 2\pi\int_0^{\pi}(|A|^2 + |B|^2)\sin(\theta)d\theta, \tag{27}$$

$$\sigma_m = 2\pi\int_0^{\pi}(1-\cos\theta)(|A|^2 + |B|^2)\sin(\theta)d\theta, \tag{28}$$

$$\sigma_v = 3\pi\int_0^{\pi}[1-(\cos\theta)^2](|A|^2 + |B|^2)\sin(\theta)d\theta, \tag{29}$$

and

$$\sigma_{tot} = \frac{4\pi}{k}\mathrm{Im}A(0). \tag{30}$$

Here, Im A(0) is the imaginary part of the non-flip scattering amplitude at $\theta = 0$. Because of this imaginary component, σ_{tot} contains both the elastic and inelastic (absorption) parts. In the present study, the inelastic cross section σ_{in} is expressed as

$$\sigma_{in} = \sigma_{tot} - \sigma_{el}. \tag{31}$$

The relativistic treatment of $e^{\pm}$ collisions enables us to calculate the polarization, which describes the difference between the measured number of scattered electrons with spin up and spin down. The expression for the Sherman function in terms of the two contributions to the scattering amplitude is given by

$$S = \frac{2\mathrm{Re}(AB^*)}{|A|^2 + |B|^2}, \tag{32}$$

which suggests that the behaviour of the scattering amplitudes A and B in Eqs. (24) and (25), respectively, determines the total polarization points with $S = \pm 1$ near the critical minima of the DCS.

The complete dependence of the scattering process on the spin variables can be obtained from the additional polarization correlations T and U [3], where

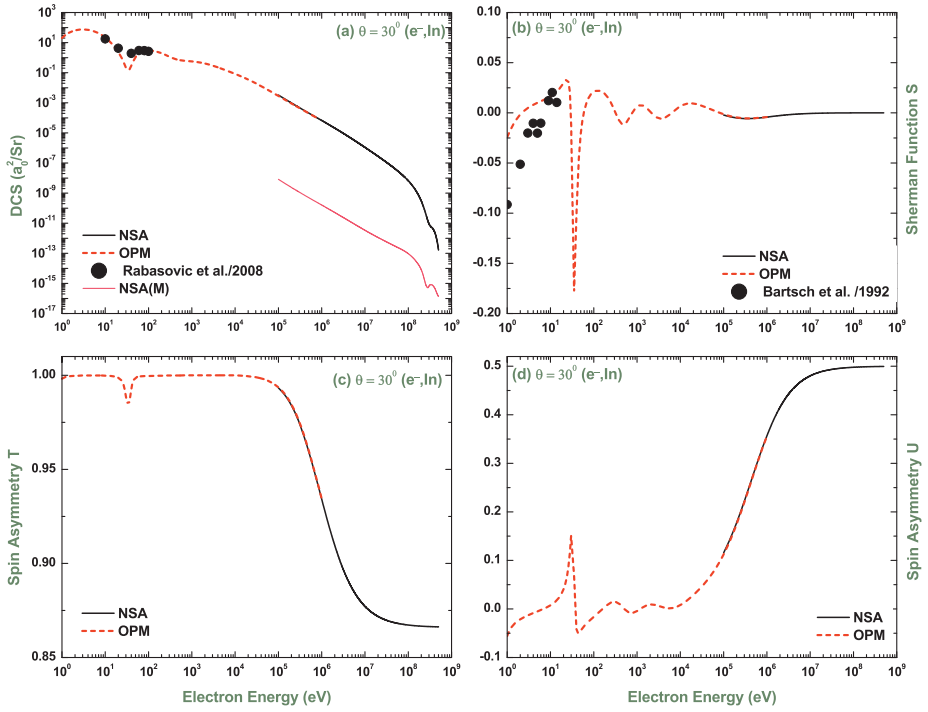

Fig. 9. Energy dependence of DCS, Sherman function S and spin-asymmetries T and U for electron-indium scattering at scattering angle $\theta = 30°$. The curves — and – – – indicate the present calculations, respectively, of the NSA and OPM approaches. The thin red line in (a) is the contribution from magnetic scattering. The symbols (•) are the experimental data of Refs. [31,32], respectively, for the DCS and S.

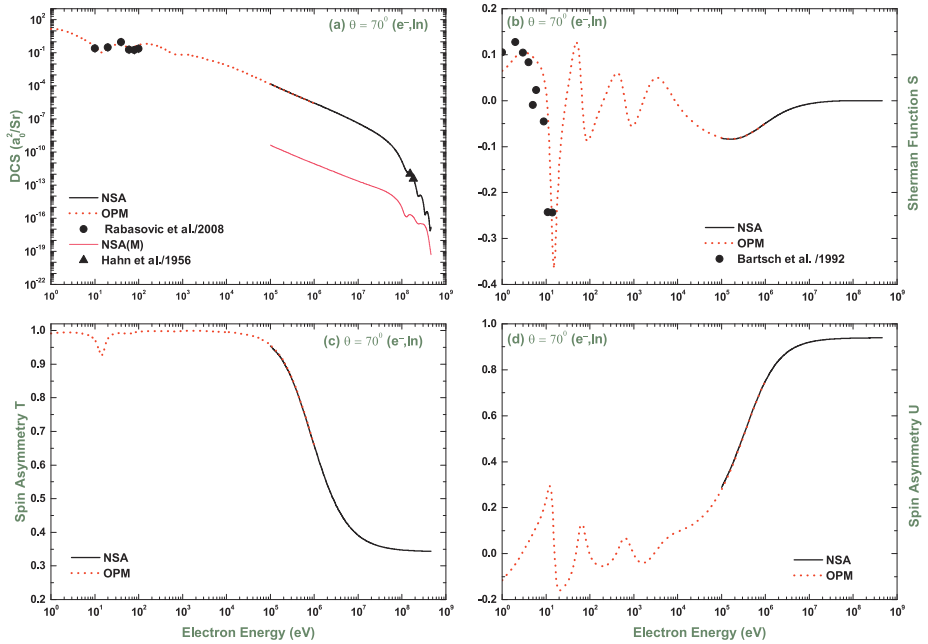

Fig. 10. Same as Fig. 9, but at scattering angle $\theta = 70°$ with additional experimental data (solid triangle) of Ref. [34].

$$T = \frac{|A|^2 - |B|^2}{|A|^2 + |B|^2}. \tag{33}$$

and

$$U = \frac{2\mathrm{Im}(AB^*)}{|A|^2 + |B|^2}. \tag{34}$$

The three spin functions S, T and U obey the following conservation relation [53]

$$S^2 + T^2 + U^2 = 1. \tag{35}$$

Hence the values of T and U depend on S and are useful indicators of the total polarization, $S(\theta) = \pm 1$.

2.3. The NSA method

For $E_i \geqslant 1$ MeV the present study employs the NSA method for obtaining the elastic scattering characteristics of electrons and positrons from ^{115}In. In the case of energies beyond 1 MeV, the projectile passes close to the nucleus, so that only the nuclear interaction part of the static potential has to be retained in the Dirac equation, which means

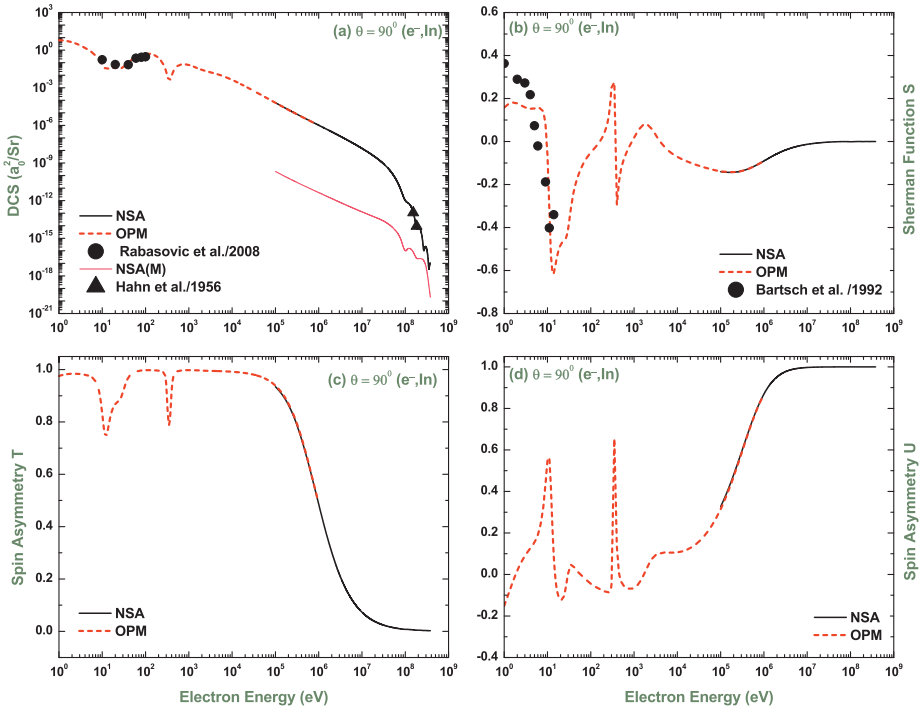

Fig. 11. Same as Fig. 9, but at scattering angle $\theta = 90°$ with additional experimental data (solid triangle) of Ref. [34].

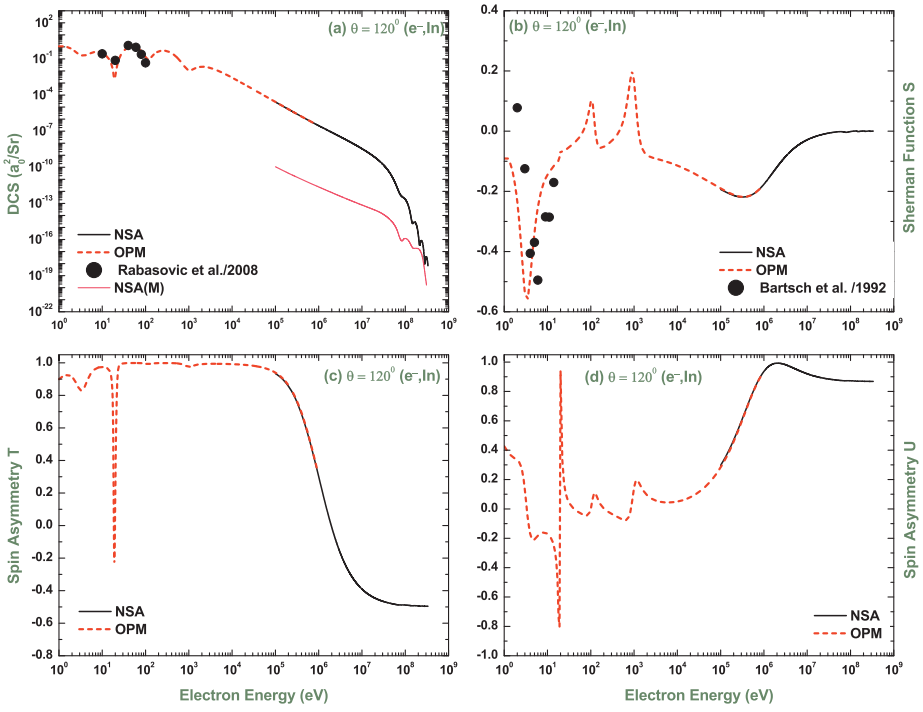

Fig. 12. Same as Fig. 9, but at scattering angle $\theta = 120°$.

replacing (7) by $V(r) = Z_0\varphi_n(r)$. This potential is generated from the Fermi-type nuclear ground-state charge distribution $\rho_n(r)$,

$$\rho_n(r) = \frac{\rho_0}{1 + e^{(r-c)/a}}, \tag{36}$$

with $\rho_0 = 0.074$ fm^{-3}, such that ρ_n is normalized to Z. For ^{115}In, the parameters are given by $c = 5.24$ fm and $a = 0.5234$ fm [34]. The potential is calculated with the help of (9).

For potential scattering, the phase shift analysis is the same as applied at low and intermediate energies, using Eqs. (24)–(26). For high energies beyond 1 MeV the sum over the phase shifts in (24) and (25) is handled by means of a threefold convergence acceleration. In this method, the singularity of A and B at $\theta = 0$ is attenuated by means of multiplying A and B with $(1 - \cos\theta)^m$, $m = 3$, and reexpanding in terms of P_l [46,47].

At energies near 50 MeV and above, magnetic effects come into play if the nucleus has spin, respectively, a magnetic moment. They arise from the current–current interaction between the lepton and the nucleus. This means that for the scattering of highly relativistic electrons or positrons from such nuclei, there are additional contributions to the

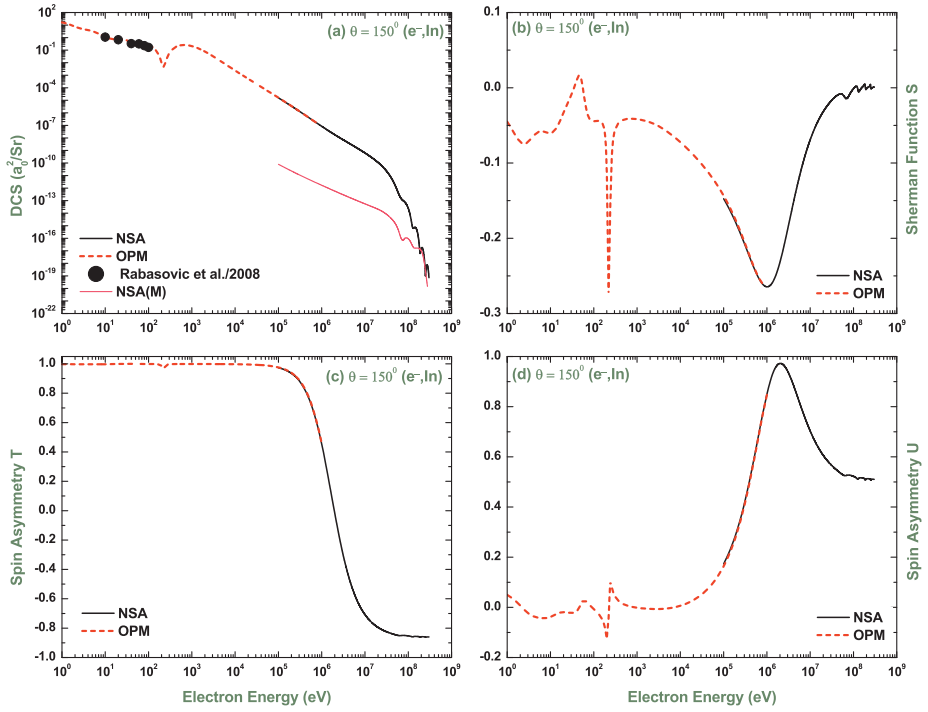

Fig. 13. Same as Fig. 9, but at scattering angle $\theta = 150°$.

transition amplitude besides the amplitude f_e for potential scattering.

For ^{115}In with $J^\pi = \frac{9^+}{2}$, magnetic transitions M_λ of multipolarity λ ($\lambda = 1, 3, ..., 2J$) can occur, where M_1 is the most important one for low momentum transfer, while the higher multipoles become the more relevant, the higher the collision energy [48]. In the DWBA formalism, the scattering amplitude has to be calculated separately for each multipole with the help of the respective nuclear transition density. These amplitudes must then be added to f_e in order to obtain the total transition amplitude. Due to the lack of accurate multipole transition densities, we are using the Born approximation to magnetic scattering instead. In this theory the DCS for unpolarized leptons is given by [23]

$$\left(\frac{d\sigma}{d\Omega}\right)_0 = |A|^2 + |B|^2 + \left(\frac{d\sigma}{d\Omega}\right)_{\rm mag}, \tag{37}$$

with

$$\left(\frac{d\sigma}{d\Omega}\right)_{\rm mag} = \frac{E^2}{c^4 q^4}(3 - \cos\theta)\,|F_T(q)|^2 \approx \sigma_{\rm Mott}\left(\frac{1}{2} + \tan^2\frac{\theta}{2}\right)|F_T(q)|^2, \tag{38}$$

where $q \approx 2\,\mathrm{k}\,\sin(\theta/2)$ is the momentum transfer, $E \approx$ kc for high energies, and $\sigma_{\rm Mott} = \frac{\cos^2\theta/2}{(2kc\sin^2\theta/2)^2}$ is the Mott cross section. Like for potential scattering, recoil is omitted in (38). The magnetic form factor $F_T(q)$ has been obtained from a fit [48] to the experimental scattering cross sections recorded at angles close to 180° (see, e.g. [49]), where magnetic scattering is largely dominant. Thus $F_T(q)$ results from the joint effect of all multipole transitions. It was shown in an investigation on spin-$\frac{1}{2}$ nuclei [4] that the Born approximation (37) is reliable as long as $(\frac{d\sigma}{d\Omega})_{\rm mag}$ is smaller than $|A|^2 + |B|^2$.

As concerns the spin asymmetries, there is, within the above approximation, no consistent way of including the magnetic contribution. With the use of a global form factor, as in (38), interference effects are disregarded. Such interference effects occur not only among the magnetic multipole transitions, but also between f_e and the magnetic scattering amplitudes. For this reason the magnetic scattering is not considered in our results for the spin asymmetries.

3. Results and discussions

3.1. Electron-indium scattering

As mentioned above, we have employed two theoretical approaches, OPM and NSA. For incident projectile energies below 10^6 eV, the OPM prescription is used, employing the HF density function. Results for the DCS, ICS, MTCS, VCS, INCS and TCS are provided up to 10^4 eV. Spin asymmetries and critical minima in the DCSs are also studied using the OPM theory. The NSA method is applied to compute the energy dependence of the DCSs and the spin asymmetries for incident energies $E_i > 10^5$ eV.

We compare in Fig. 1(a) our OPM calculations of ICS for electron-indium elastic scattering with the experimental data of Rabasović et al. [31] and theoretical predictions of Rabasović et al. [31], Öztürk et al. [35] and Mayol and Salvat [38]. We see a close agreement between them and with experiment, except for a slight overestimation of the two experimental data points at around $E_i \simeq 100$ eV. However, in the vicinity of 50 eV, two shallow structures are found in the calculations of Rabasović et al. [31] that are not clearly seen in our calculations.

The MTCS and VCS calculated for the elastic scattering of electrons from indium are presented, respectively, in Fig. 1(b) and (c). As seen from these figures, our calculations reproduce the pattern of the energy dependence of the experimental cross sections [31], the number of minima, and their energy positions except again a little overestimation in absolute values. The predictions of Mayol and Salvat [38], however, differ significantly from both the experimental and the present results in the energy domain 100–1000 eV. The difference in the two calculations might originate from the use of different potential components and procedures of calculations.

In Fig. 1(d) we present our INCS results in comparison with the experimental data and the theoretical values of Rabasović et al. [31]. It is evident from this figure that our calculations substantially overestimate the experimental data and theoretical predictions at lower energies of $E_i \leqslant 40$ eV. The difference between the present results and those of [31] might be, at least partly, attributed to the use of different potentials and methods in the aforesaid two calculations.

Fig. 1(e) presents our TCS results in comparison with the predictions

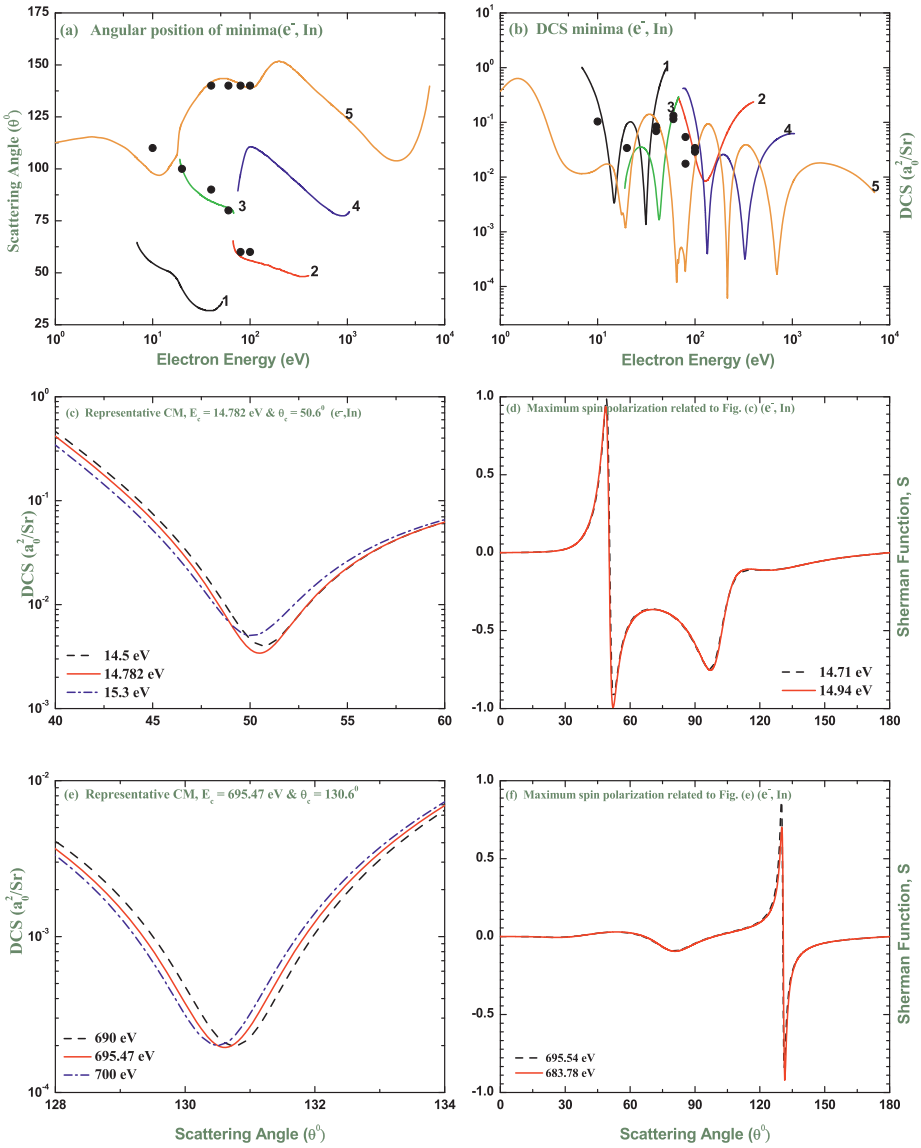

Fig. 14. Energy dependence of angular positions and DCS values of deep minima for electron-indium scattering. Also are shown the angular dependence of DCS and S for some incident energies in the vicinity of the critical minima [E_c = 14.782 eV; θ_c = 50.6°] and [E_c = 695.47 eV; θ_c = 130.6°].

of Rabasović et al. [31]. So far as we are aware, no experimental data are available for this scattering characteristics. The comparison of the theories shows that the results from [31] continue to underestimate the present results up to E_i = 100 eV. Again this difference might stem from the same causes as touched upon for INCS in Fig. 1(d). It is worth mentioning that in the reported Rabasović et al. [31] calculations, more than 60% of the contribution to their TCS originates from ICS, which is, according to Fig.1a, significantly lower than the present results in this energy region.

Our OPM calculations of the DCS for electron-indium elastic scattering at impact energies in the range $10 \leqslant E_i \leqslant 10^4$ eV are shown in Figs. 2–5. The oscillations of the DCS with angle (or energy) are the so-called Ramsauer-Townsend structures (see, e.g., the review by Lucas et al. [50]). They originate from interference effects caused by the leptons scattering from the individual electrons of the atom. The structures disappear when the collision becomes so energetic that the lepton-atom interactions occur inside the K-shell (above 1 keV). As seen in these figures, the number of minima in our DCS distributions varies with energy from 2 at E_i = 10 eV to 3 at $20 \leqslant E_i \leqslant 50$ eV and again to 2 at $60 \leqslant E_i \leqslant 80$ eV. The DCSs again reveal 3 minima at $100 \leqslant E_i \leqslant 400$ eV and 2 minima at $500 \leqslant E_i \leqslant 1000$ eV. With a further increase in the collision energy to $2000 \leqslant E_i \leqslant 3000$ eV, the number of minima reduces to 1. For $E_i \geqslant 4000$ eV, the DCS decreases monotonously with energy, without yielding any minimum or maximum.

The present DCS results are compared with the experimental data of Rabasović et al. [31] at E_i = 10, 20, 40, 60, 80 and 100 eV, and also with the calculations of Rabasović et al. [31] at $10 \leqslant E_i \leqslant 300$ eV and Öztürk et al. [35] at E_i = 50, 100, 200, 500, 1000 and 2000 eV. For E_i > 2000 eV, there are neither any measurements nor any other calculation of the DCS available in the literature for comparison. It is anticipated that this investigation might motivate future experimental as well as theoretical studies.

The comparison shows that the present DCS curves agree fairly well with the experimental data apart from differences in magnitude in the vicinity of the deep minima. However, those of Rabasović et al. [31] agree better with the experimental data. It is worth mentioning that Rabasović et al. [31] used energy dependent parameters $W_i(E)$ for the absorption potentials VA_i, i = 1–3 and $\beta(E)$ in their Eqs. (3) and (4). It is clear from Table 1 of Ref. [31] that for each energy they used different adjustable parameters. Besides, the experimental data are normalized at 20 deg. to their SEPAS. (VA_3) calculations. On the other hand, the present work uses one value for the generalized absorption

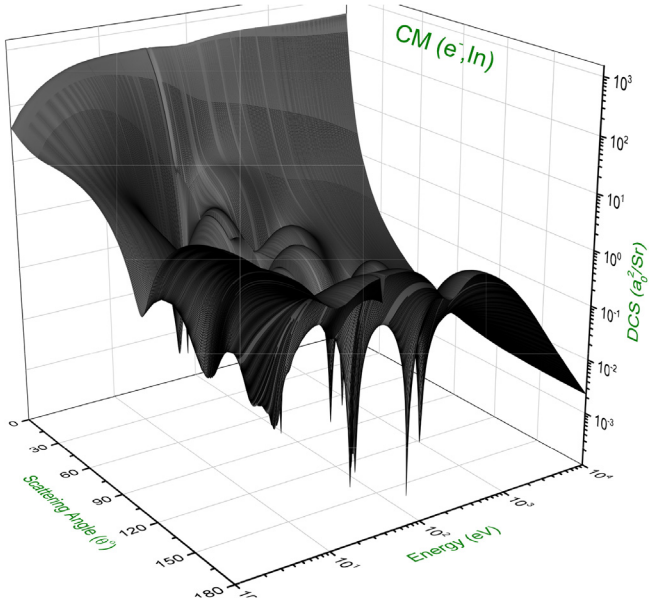

Fig. 15. A three-dimensional (3D) plot of the present DCS for electron-indium scattering.

Table 2
Maximum spin polarization with their positions, and deviations in energy ΔE and angle $\Delta\theta$ from the respective CM positions for e^-- In elastic scattering.

E_c (eV)	θ_c (deg.)	$S(\theta)$	E_d (eV)	θ_d (deg.)	$\pm\Delta E$ (eV)	$\pm\theta_d$ (deg.)
6.802	105.4	+0.541544	4.82	108.2	1.982	2.8
		−0.999782	7.41	105.0	0.608	0.4
14.782	50.6	+0.998330	14.71	49.0	0.072	1.6
		−0.998238	14.94	52.2	0.158	1.6
17.68	106.6	+0.939938	18.36	113.4	0.68	6.8
		−0.999771	17.35	100.6	0.33	6.0
19.32	120.2	+0.937807	18.46	114.2	0.86	6.0
		−0.999018	19.85	123.0	0.53	2.8
31.32	32.6	+0.997191	30.52	33.0	0.8	0.4
		−0.878687	32.11	32.2	0.79	0.4
42.75	83.8	+0.990479	43.18	83.0	0.43	0.8
		−0.988026	42.22	84.6	0.53	0.8
64.842	142.6	+0.922400	63.8	142.6	1.042	0.0
		−0.922057	66.09	142.6	1.248	0.0
67.45	142.2	+0.393140	64.87	142.2	2.58	0.0
		−0.912895	68.9	142.2	1.45	0.0
79.46	140.6	+0.999420	80.59	140.2	1.13	0.4
		−0.998850	78.17	141.0	1.29	0.4
133.93	107.8	+0.999487	130.83	108.2	3.1	0.4
		−0.977497	137.47	107.4	3.54	0.4
215.41	151.4	+0.769096	214.01	151.8	1.4	0.4
		−0.763636	217.01	151.0	1.6	0.4
325.5	92.2	+0.999854	323.37	91.8	2.13	0.4
		−0.972910	327.77	92.6	2.27	0.4
695.47	130.6	+0.901809	695.54	130.2	0.07	0.4
		−0.998777	683.78	131.4	11.69	0.8

parameter A_{abs} over the whole range of energies. So it is not unexpected that the results of Rabasović et al. should produce better agreement with their own measurements than the present results.

The poor agreement of our results with the experiment at the lower impact energies (⩽20 eV) may come from the onset of the inelastic threshold which interplays between the real and imaginary components of the optical potential due to dispersion. Moreover, the uncertainty of the atomic dipole polarizability could produce some discrepancy between the calculated and the measured values. Nonetheless, at 10 eV, our DCS provides a reasonable agreement with the data for the lower and the higher scattering angles, whereas the calculations of [31] disagree significantly and fail to show even the oscillatory behavior.

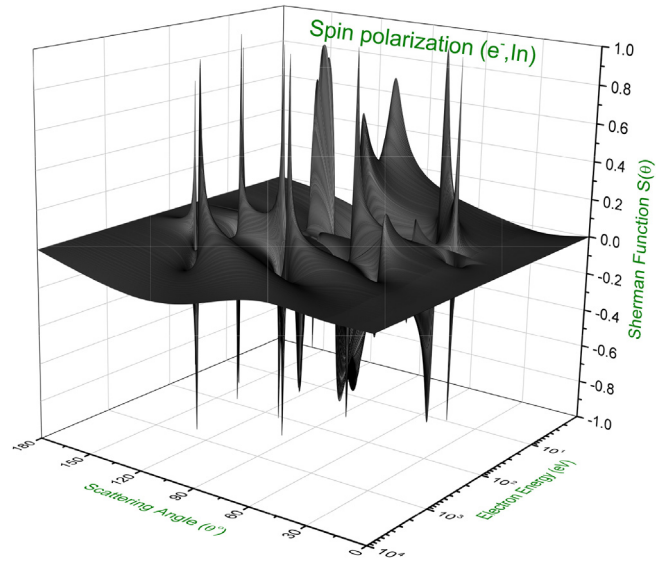

Fig. 16. A 3D plot of the Sherman function for electron-indium scattering from the present results.

A comparison among the theoretical predictions shows that the present calculations and those of Rabasović et al. [31] and Öztürk et al. [35] exhibit resonance structures at about the same scattering angles but with little variations in the magnitude. Up to the energy 20 eV, as evident from Figs. 2(a) and (b), the present DCS values are lower than those of Rabasović et al. [31] by roughly a factor of 2–2.5 at most of the angles. Beyond this energy, the present DCS values are higher than those of [31] by a factor of 1.5–3.0, with few exceptions. At the smaller energies (below 30 eV), the present work produces an extra minimum in the backward hemisphere. Öztürk et al. [35] predicted lower DCS values in and around 0–12 degree by a factor of 5–10 and, on the other hand, largely higher values than the present calculation over the remaining angular domain. In the overall assessment, their DCS values [35] (Figs. 2–5) are, more often than not, higher by a factor of 2 than the present calculation and a factor of 4 than those of Rabasović et al. [31]. These variations signify the sensitivity of the theoretical models involving different interaction potentials. We recall that for the interaction of an electron with the indium atom, all three models mentioned above use the optical potential (OP), but with different components. For example, while the OP in the present study and in Ref. [31] contains both the real and absorption parts, the OP in Ref. [35] contains the real part only. In our calculations and in those of [35], the real part of OP comprises the static, the exchange and the polarization potentials while in Ref. [31] the real part includes additionally the spin-orbit potential. The overestimation of the DCS values in Ref. [35] may be due to the absence of an absorption potential in their OP. Because of the presence of inelastic processes the absorption potential has a significant effect on the DCS curves, especially at the minima and maxima for the larger scattering angles.

In Figs. 6–8 we compare our OPM results of the Sherman function S for electrons elastically scattered from indium atoms for incident energies $1 \leqslant E_i \leqslant 400$ eV. The present results are compared with the only measured data of Bartsch et al. [32] at E_i = 1–14 eV. They are also compared with the close-coupling calculations of Bostock et al. [22] at E_i = 1–14 eV and Bartschat et al. [37] at E_i = 1–3 eV. We found in the literature neither any measurements nor theoretical calculations of S at higher energies ($E_i \geqslant 20$ eV) for electron-indium elastic scattering to compare with.

The comparison at low energies shows that, unlike for the DCSs, our spin asymmetry results do not agree with experiment or other calculations. This can be explained in the following way. Before the onset of the inelastic threshold at 5.8 eV, there may be an interplay between the

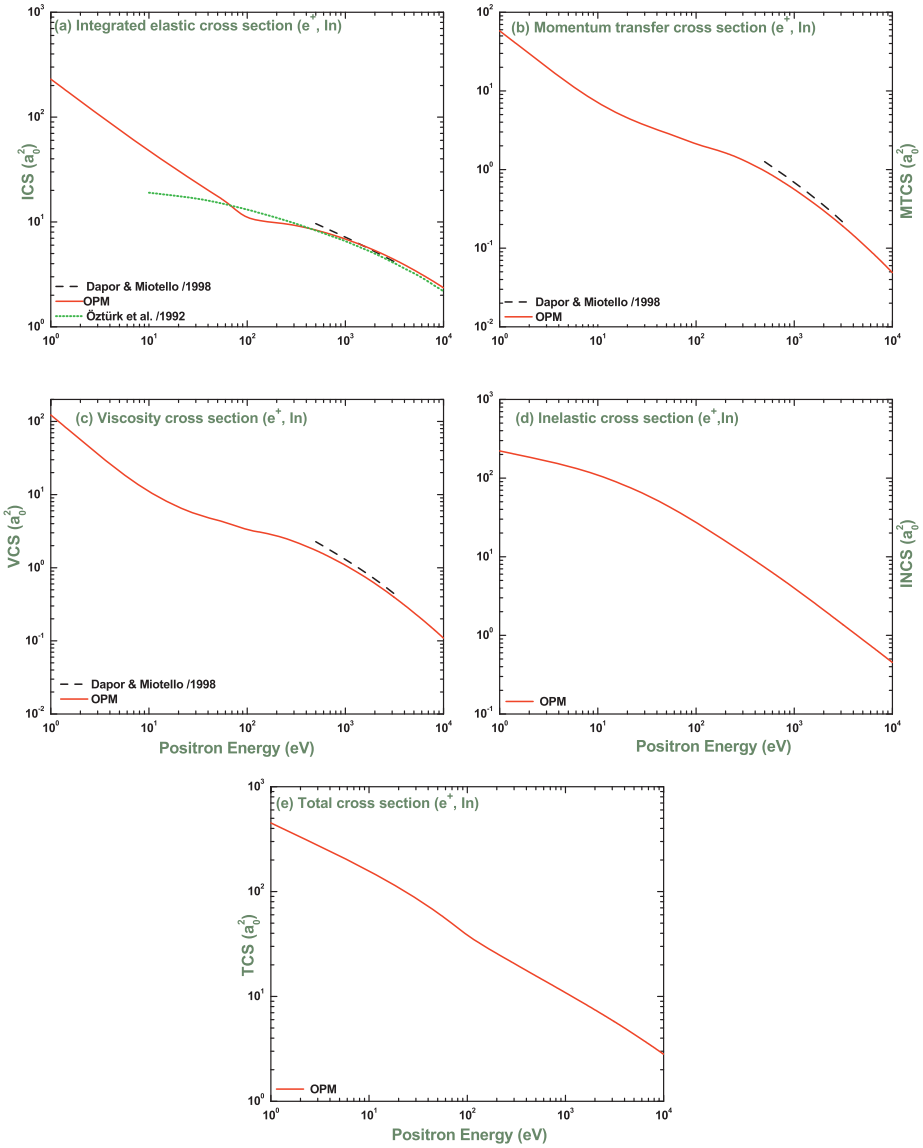

Fig. 17. Energy dependence of the ICS, MTCS, VCS, INCS and TCS for positron-indium scattering: — line, present OPM calculations; – – – line, Ref. [36]; ⋯ line, Ref. [35].

real and the imaginary parts of the OP due to the dispersion effect, leading to a deviation from the smooth variation of the OP parameters with energy. This feature is not considered in the present study. Also there will be a substantial contribution of the resonance elastic scattering corresponding to the isolated levels of a composite system that can not be modeled accurately in the OPM approach. Nonetheless, the present calculations exhibit oscillations at about the same scattering angles, while the differences are largest at the extrema of S. Also a reasonable quantitative agreement with the experiment is seen at lower scattering angles up to $\theta = 90°$ for $E_i < 10$ eV.

Figs. 9–13 present the energy dependence of the DCS of the elastic electron-indium scattering over the energy range 1 eV $\leqslant E_i \leqslant$0.5 GeV at three forward scattering angles ($\theta = 30°$, 70° and 90°) and two backward angles ($\theta = 120°$ and 150°). The curve designated by NSA(M) represents the cross section due to the magnetic scattering only. It is seen that the magnetic effect is, particularly at the forward angles, very small compared to the electrostatic effect of the nucleus., except at ultrahigh energies.

From Figs. 9–13 it follows that the OPM and the NSA predictions of the DCS merge smoothly at around 1 MeV. Strong Ramsauer-Townsend structures are observed at all scattering angles for kinetic energies $E_i < 1$ keV. Beyond 1 keV up to about 50 MeV, the DCS declines monotonously with E_i. This is expected because it is the pure Coulomb field of the nucleus which acts in this energy regime. At ultra-relativistic energies ($E_i \simeq$ 100 MeV), the structures reappear due to the diffraction effects resulting from the projectile scattering by the individual protons of the indium target nucleus. One can also see that the low-energy structures gradually fade out as E_i advances towards the M-subshell binding energies (which are located at 0.4 − 0.8 keV). In the case of high energies, the structures reappear and follow basically a $j_1(qR_N)$ pattern [51], where R_N is the nuclear radius, $q \approx 2k_i \sin(\theta/2)$ is the momentum transferred to the nucleus, and j_1 is a spherical Bessel function.

The OPM predictions of the DCS are compared with the experimental data of Rabasović et al. [31], as discussed earlier, at some fixed angles. This is done to examine the energy dependence of the DCS at a particular angle. The NSA results are compared with the data measured by Hahn et al. [34] at $\theta = 70°$ and 90°. The comparison shows that a good agreement with experiment is achieved by the NSA results. No other experimental or theoretical values of the DCS, for electron scattering at the higher energies, are available to compare with the NSA results.

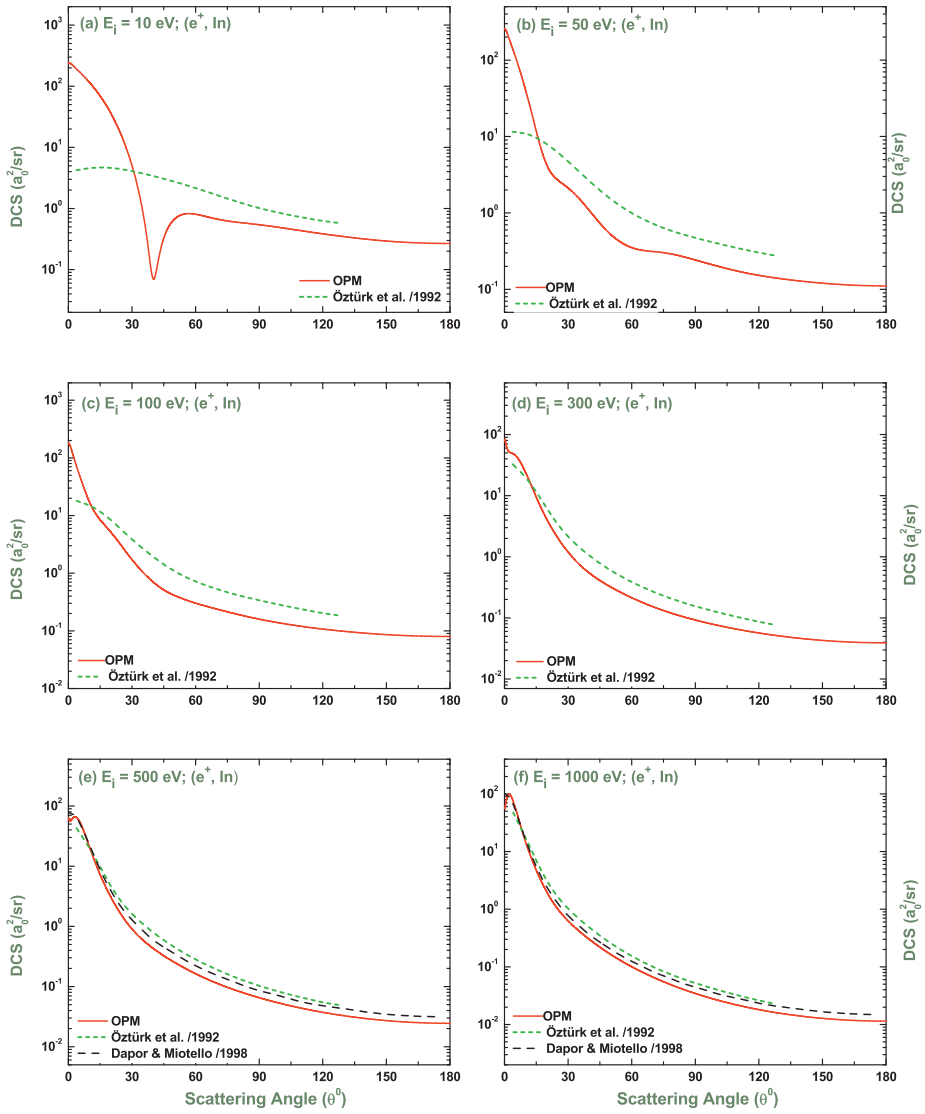

Fig. 18. Angle DCS for elastic scattering of 10, 50, 100, 300, 500 and 1000 eV positrons from indium in units of a_o^2/Sr: solid curves, present OPM calculations; short-dashed curves, Ref. [35]; broken curves, Ref. [36].

In Figs. 9–13 we also present the energy dependence of the Sherman function S and the spin asymmetries T and U, respectively, in the subfigures (b), (c) and (d) of each of these figures. Like in the case of the DCS curves, the OPM and NSA results for all spin-polarization parameters merge smoothly at the matching point of about 1 MeV. The OPM results of S are compared again with the measured data of Bartsch et al. [32], which have been discussed earlier. However, no data for S, neither experimental nor theoretical, are available to compare with the NSA predictions in the high-energy domain. Moreover, we are not aware of any measurements or any calculations for T and U to compare with our results.

It is evident in Figs. 9–13 that the Ramsauer-Townsend structures which appear in S below 1 keV relate to those of the DCS curves. However, the structures in S are much stronger than those observed in the DCS. These pronounced structures in S are due to the greater sensitivity of the spin polarization to interference effects, and thus to the choice of the potentials and methods for the calculations. It is also observed that, in the forward hemisphere, the magnitude of S increases with scattering angle for all energies. The picture is opposite in the case of backward scattering angles. This observation indicates that the nuclear electrostatic field becomes stronger at a smaller projectile-nucleus distance.

The angular positions of the DCS minima are plotted as a function of the incident energy in Fig. 14(a). It is evident from this figure that the low-angle minima (curves 1 and 2) are not found in the DCSs below 6.9 eV, but maintain their appearance up to 400 eV. The angular positions of these minima vary from 64.6° at 6.9 eV to 48.6° at 400 eV reaching a minimum at 31.8°. The intermediate-angle minima (curves 3 and 4) in the DCS are seen to appear for collision energies $19 \leqslant E_i \leqslant 1050$ eV. The high-angle minima (curve 5), on the other hand, are present at all energies below 7000 eV with the angular positions varying between 96° and 151.8°. Compared to the experimental data from Ref. [31], our results show a close agreement with a slight underestimation for the intermediate scattering angles.

Fig. 14(b) displays the energy dependence of the deep DCS minima. The positions of these deep minima have been traced with the help of the DCS minima in the angular distribution shown in Fig. 14(a). As seen in Fig. 14(b), the present study predicts a total of 14 deep minima in the DCS distributions. In the low-angle minimum region, corresponding to curves 1 and 2, there are three such deep minima located at the critical energies E_c = 14.782, 31.32 and 128 eV. Three deep minima at E_c = 42.75, 133.93 and 325.5 eV are visible in the intermediate-angle minimum regions, depicted in curves 3 and 4. In the high-angle minimum region (curve 5), there are 8 deep minima at E_c = 6.802,

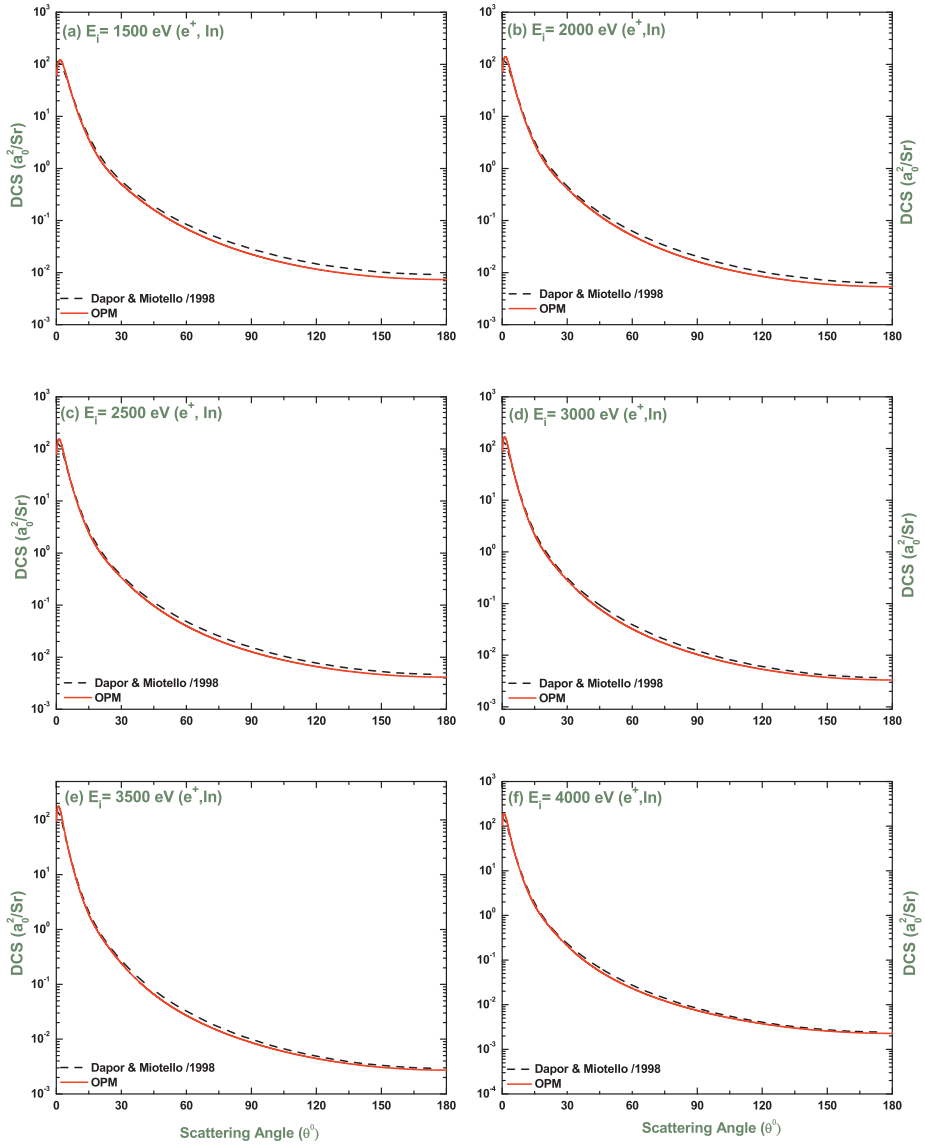

Fig. 19. Same as Fig. 16, but at impact energies of 1500, 2000, 2500, 3000, 3500 and 4000 eV. – – – curves are the calculations of Dapor and Miotello [36].

17.68, 19.32, 64.842, 67.45, 79.46, 215.41 and 695.47 eV.

In the vicinity of a CM, the non-flip scattering amplitude A should approach zero [5]. Therefore, an important criterion for a minimum point in the energy-dependent DCS to be a critical one is that the magnitude of the spin-flip amplitude must be larger than that of the non-flip amplitude, i.e. $|B| \gg |A|$. In view of this criterion, among the 14 deep minima observed in Fig. 14(b), only one minimum, located at $E = 128$ eV, at the critical angle $\theta_c = 54.6°$ with $|A| = 4.6 \times 10^{-10}$ and $|B| = 1.4 \times 10^{-10}$, does not qualify to be a CM. The qualified 13 CMs along with their respective E_c and θ_c are listed in Table 1. The three-dimensional (3D) plot of the DCS, in Fig. 15, clearly shows the positions of these CM in terms of impact energy as well as scattering angle. The highest critical energy occurs for ($E_c = 695.47$ eV; $\theta_c = 130.6°$) whereas the highest critical angle shows up at ($E_c = 215.41$ eV; $\theta_c = 151.4°$).

For electron-indium scattering, Rabasović et al. [31] obtained 7 CMs by using their SEPSo (without absorption) approach and 6 CMs by SEPASo (with absorption) approach. The positions of those CMs are also displayed in Table 1. It is evident from this table that the angular positions of the CMs predicted in the present study produce an overall good agreement with those obtained by Rabasović et al. [31]. There is no available experimental measurements on CM for this scattering system to compare our results with.

Two more important features of the CM are: (i) at a CM the DCS attains a local minimum, (ii) the position of a CM is the only one for which the Sherman function attains in its vicinity both its maximum and minimum. In order to illustrate the effectiveness of our present model the angular dependence of DCS and S for some incident energies in the vicinity of the two critical minima [$E_c = 14.782$ eV; $\theta_c = 50.6°$] and [$E_c = 695.47$ eV; $\theta_c = 130.6°$] are, respectively, presented in Figs. 14(c) and (d) and 14(e) and (f). From Fig. 14(c) it follows that the DCS attains its minimum exactly at 14.782 eV. The DCS gets higher if the energy is slightly increased to 15.3 eV or decreased to 14.5 eV. A similar scenario is echoed in Fig. 14(e), where DCS is the lowest at 695.47 eV, as compared to the values at 700.0 eV and 690 eV in its proximity. In case of the Sherman function, Fig. 14(d) shows that, in the vicinity of [$E_c = 14.782$ eV; $\theta_c = 50.6°$], the present S values vary from $+0.99$ at 47° to -1.0 at 50°. Also in the case of [$E_c = 695.47$ eV; $\theta_c = 130.6°$] in Fig. 14(f), we observe a similar behavior. All these results demonstrate the efficacy of the present electron-atom optical potential in determining the CM positions accurately.

The significance of finding a CM position is that in its neighborhood the scattered electrons acquires total polarization ($S = \pm 1$). In the vicinity of each CM, obtained in the present study, we have calculated the energy E_d and angle θ_d at which the polarization reaches extremal

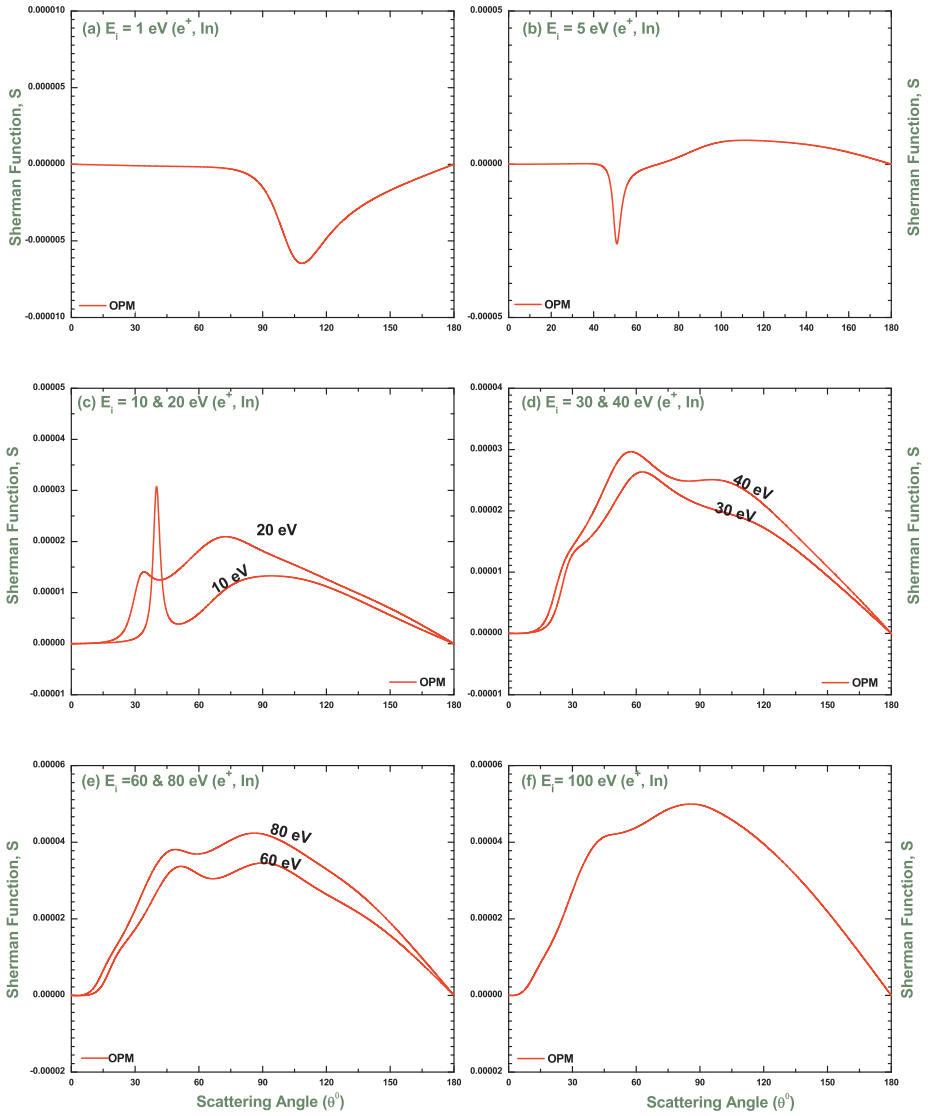

Fig. 20. The Sherman function S for elastic scattering of 1, 5, 10, 20, 30, 40, 60, 80 and 100 eV positrons from indium predicted by the present OPM approach.

values of both signs. We have found a total of 26 such points, which are listed in Table 2. Also shown are the positions of these maximum polarization points by a 3D plot in Fig. 16. It is evident from Table 2 that a large polarization ($S \geqslant 90\%$) is achieved at 22 deepest points (out of 26) which can be considered as total polarization points. At the remaining 4 points, the polarization varies between $0.4 \leqslant |S| \leqslant 0.8$. According to Walker [52], however, the points with $|S| > 0.5$ could also be considered as having total polarization.

At the extrema of the spin polarization one has the following properties: (i) the sum of the energy widths of the positive and negative excursions, ΔE^p and ΔE^n, is related to the width in energy of the DCS valley at the corresponding CM position. (ii) Similarly, the sum of the angular widths $\Delta\theta^p$ and $\Delta\theta^n$ is equal to the angular width of the DCS at this CM position. In addition, we have calculated the energy widths ΔE denoting the energy difference between E_c and E_d, and the angular widths $\Delta\theta$ denoting the angle difference between θ_c and θ_d for each point at which the extremum value of polarization is attained. They are also presented in Table 2. If we consider the high-angle CM at $E_c = 64.842$ eV, $\theta_c = 142.6°$, the corresponding $S = 0.922400$ at $E_d = 63.8$ eV with $\Delta E^p = 64.842 - 63.8 = 1.042$ eV and $\Delta\theta^p = 142.6 - 142.6 = 0.0°$, while $S = -0.922057$ at $E_d = 66.09$ eV with $\Delta E^n = 66.09 - 64.842 = 1.248$ eV and $\Delta\theta^n = 142.6 - 142.6 = 0.0°$. Therefore, the widths of the DCS valley are $1.042 + 1.248 = 2.290$ eV along the energy axis and $0.0° + 0.0° = 0.0°$ along the angular axis. The latter suggests that the angular DCS distribution at a CM and the corresponding S distribution near the extrema of S are both very sharp.

3.2. Positron-indium scattering

The present OPM results of ICS, MTCS, VCS, INCS and TCS for positron-indium scattering are displayed in Fig. 17. It is noticeable that the energy variations of ICS, MTCS and VCS for positron scattering are considerably different in shape from their electron counterparts in Fig.1. In particular, the energy dependence of the MTCS and VCS for electron scattering between $E_i = 10$ and 100 eV shows a maxima and minima pattern, which is absent in the case of positron scattering. This feature might be due to the differences in electron-atom and positron-atom interacting potentials. We would like to recall that the static potential is repulsive and the exchange potential is absent for positron projectiles.

We have not found any experimental data for the above scattering observables. However, the present results can be compared with the theoretical predictions of Öztürk et al. [35], available for ICS, and those of Dapor and Miotello [36], available for ICS, MTCS and VCS. As seen in Fig. 17(a) for the ICS results, our OPM calculations produce nice agreement with the other two calculations [35,36] at $E_i > 10^3$ eV.

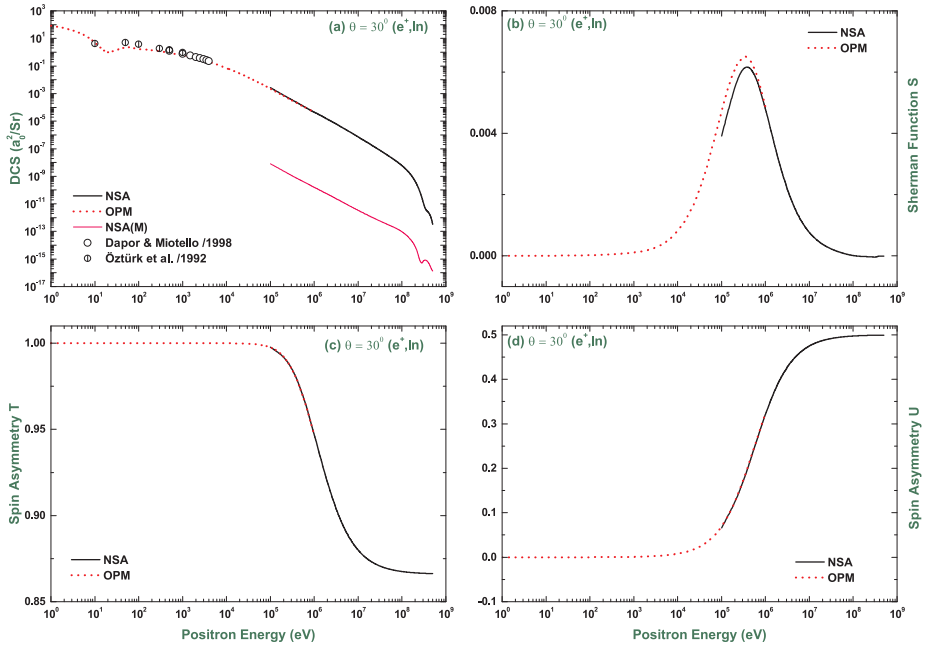

Fig. 21. Energy dependence of DCS, S, T and U for positron-indium scattering at scattering angle $\theta = 30°$. The thick solid and dashed lines are the present calculations, respectively, due to the NSA and OPM approaches. The thin red line in (a) is the contribution from magnetic scattering. The symbols are the experimental data from Ref. [36] and Ref. [35].

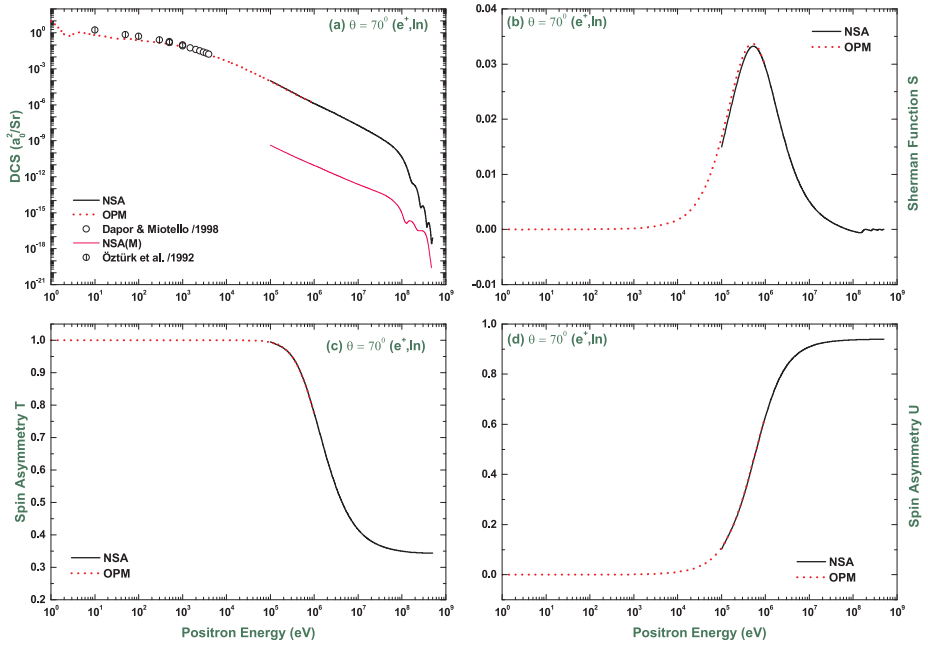

Fig. 22. Same as Fig. 19, but at scattering angle $\theta = 70°$.

However, a noticeable disagreement, both qualitatively and quantitatively, is seen between the OPM results and those of Ref. [35] for projectile energies $E_i \leqslant 700$ eV. The present results of MTCS and VCS, depicted in Fig. 17(b) and (c), show the same energy variation as those of Ref. [36], but with a little difference in magnitude. This may come from the different interacting potentials used in the models. The energy variations of INCS and TCS are almost the same as those from electron scattering. To the best of our knowledge, there are neither experimental data nor theoretical results for these quantities available in the literature to compare with.

The angular dependence of the DCS for the elastic scattering of positrons from indium at impact energies 10 eV$\leqslant E_i \leqslant$4000 eV is presented in Figs. 18 and 19. As seen in these figures, the DCS curves for positrons scattering show a fewer number of maxima and minima than those for electron impact. Only one significant minimum is seen at $E_i = 10$ eV in Fig. 18(a). For incident energies 50 eV$\leqslant E_i \leqslant$100 eV, see Figs. 18 (b) and (c), only shallow minima are observed at the lower scattering angles. The DCS decreases monotonously at $E_i = 300$ eV and beyond.

So far as we are aware, there are no experimental data of the DCS for positron-indium scattering to compare our results with. Theoretical calculations of Öztürk et al. [35] at 10 eV$\leqslant E_i \leqslant$1000 eV, and Dapor and Miotello [36] at 1000 eV$\leqslant E_i \leqslant$4000 eV are included in the figures. The comparison shows that the present results agree very well with those of

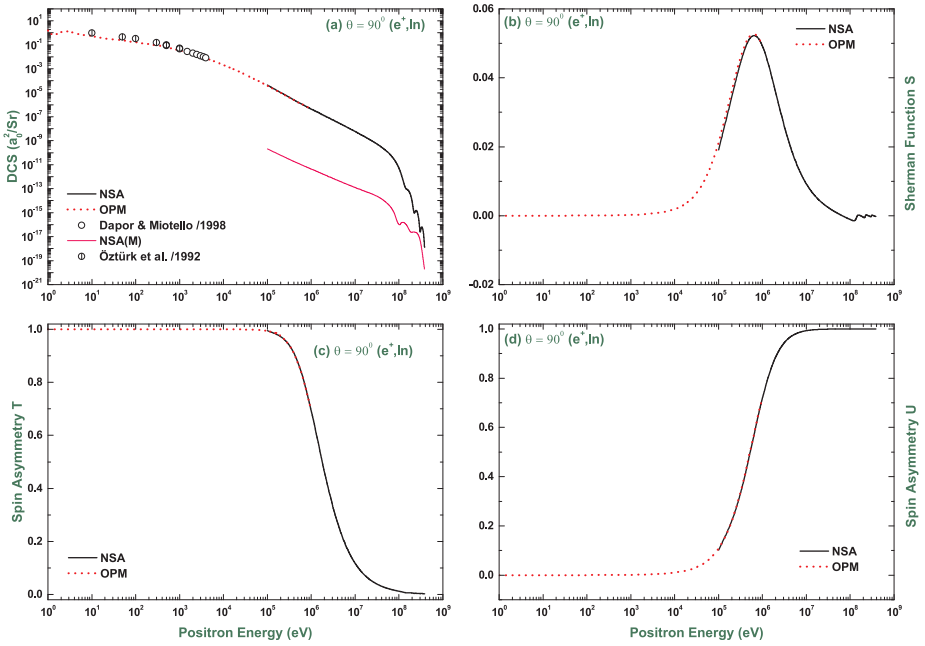

Fig. 23. Same as Fig. 19, but at scattering angle $\theta = 90°$.

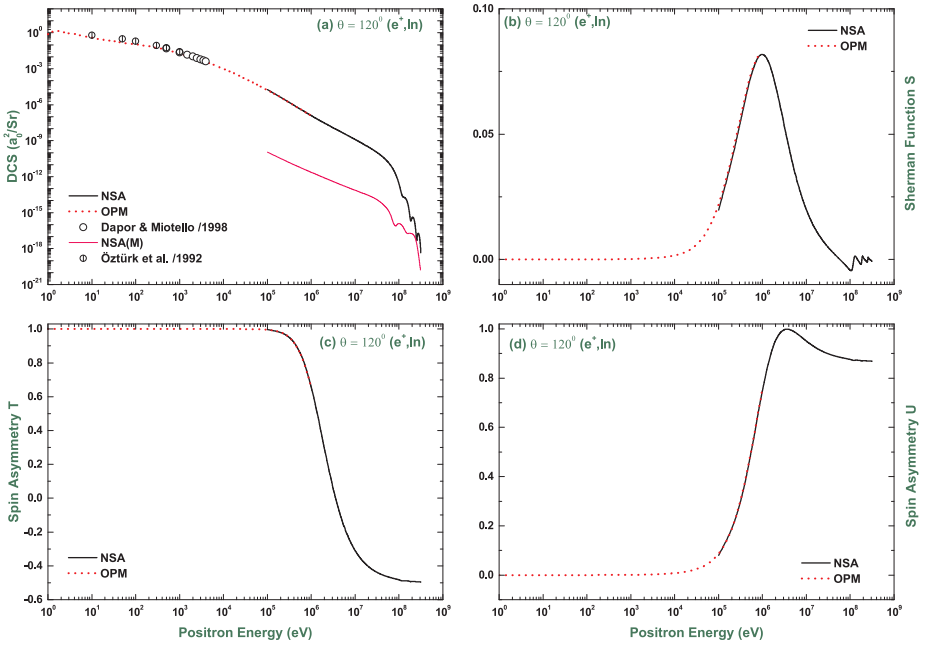

Fig. 24. Same as Fig. 19, but at scattering angle $\theta = 120°$.

Dapor and Miotello [36] at all impact energies. An overall agreement of the angular dependence is also seen between the calculations of ours and those of Öztürk et al. [35] except at 10 eV and at the foremost angles. In our predictions, at $E_i = 10$ eV, we observe a prominent minimum that is not present in the results of Ref. [35].

For positron-indium scattering, the angular dependence of the Sherman function at impact energies 1 eV$\leqslant E_i \leqslant$100 eV, calculated using our OPM approach, is displayed in Fig. 20. As apparent in this figure, our calculations display fluctuations with minima and maxima, which are stronger in amplitude at higher energies. Even so, unlike in the case of electron scattering from indium, positron scattering from indium shows a negligible amount of polarization in the scattered beam. As the spin polarization depends on the spin-orbit interaction as well as on the spatial interaction potential these tiny values of spin polarization indicate that the interaction between the positrons and the indium atoms is much weaker than in the case of electron impact. The lack of experimental and any other theoretical results precludes any comparison.

Figs. 21–25 show the energy dependence of the DCS and of the corresponding Sherman function as well as the spin asymmetries T and U for positron scattering calculated using both OPM and NSA methods at five scattering angles 30°, 70°, 90°, 120° and 150°. Similar to the case of electron scattering, both OPM and NSA predictions of the above scattering quantities merge nicely at about 1 MeV. It is also seen in the DCS curves that minor structures appear at lower scattering angles, and that they fade with the increase of energy. Like for electron impact, there are fluctuations of the DCS at ultra-relativistic energies above 100 MeV for all angles. These high-energy oscillations are also present

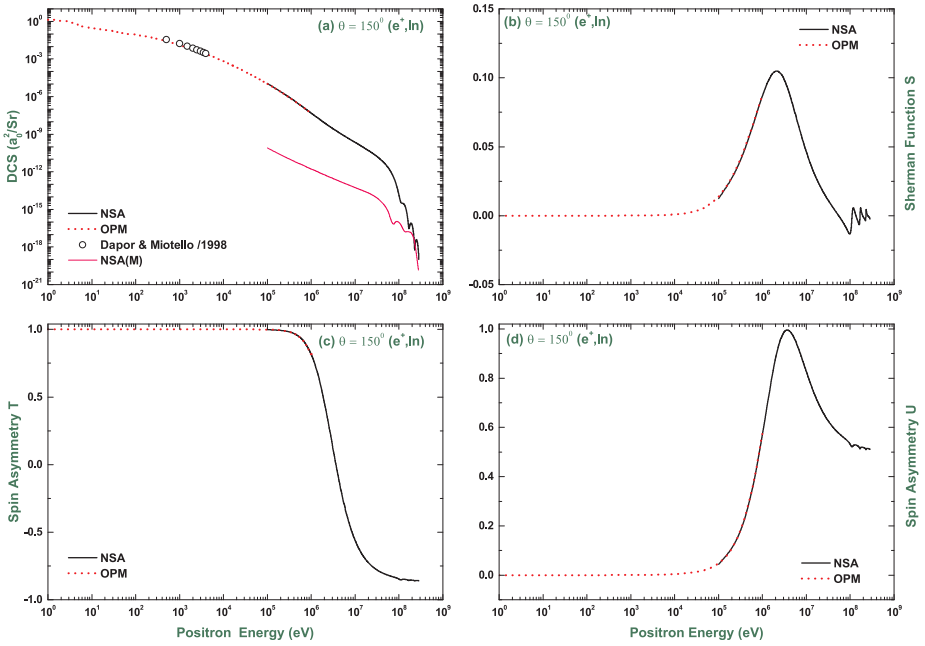

Fig. 25. Same as Fig. 19, but at scattering angle $\theta = 150°$.

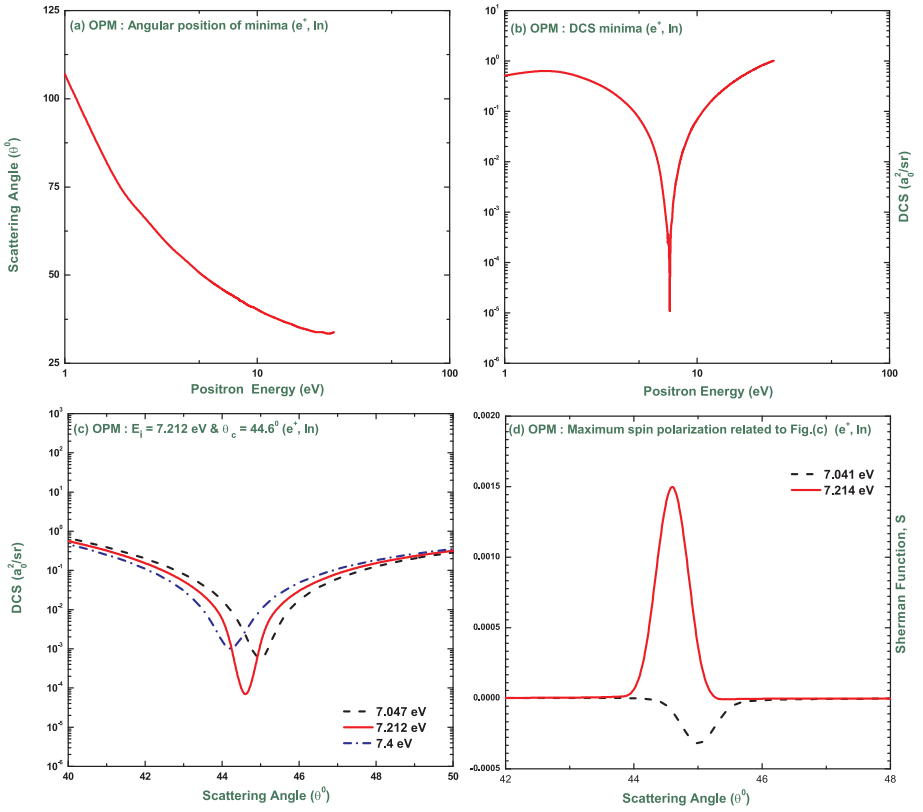

Fig. 26. Energy dependence of angular positions and DCS values of deep minima for positron-indium scattering. Also are shown the angular dependence of DCS and S for some incident energies in the vicinity of the deep minima [$E_c = 7.212$ eV; $\theta_c = 44.6°$].

for the Sherman function. There is, in addition, one pronounced maximum in S near 1 MeV, which increases with scattering angle.

Fig. 26 provides the properties of the deep DCS minima, similar to Fig. 14, but for positron scattering. As seen in Fig. 26(a), the positron minima occur up to around 30 eV with the angular position varying from $\theta = 30°$ to 110°. With the help of this angular dependence of the DCS minima we have found two deep minima, which are depicted in Fig. 26(b). The critical energy and angular positions of these deep minima are presented in Table 3. However, none of these two minima qualifies as CM point because the magnitude of the non-flip scattering amplitude $|A|$ is greater than that of the spin-flip scattering amplitude $|B|$. Albeit the magnitude of $|A|$ always attains its lowest value at these deep minima.

In Figs. 26 (c) and (d) we present, respectively, the angular

Table 3
The positions of DCS deep minima for the elastic e^+-In scattering using our OPM.

E_d (eV)	θ_d (deg.)	$\lvert A(\theta)\rvert^2$ (a_0^2/Sr)	$\lvert B(\theta)\rvert^2$ (a_0^2/Sr)
7.047	45.0	2.49E−04	1.41E−11
7.212	44.6	1.08E−05	1.40E−11

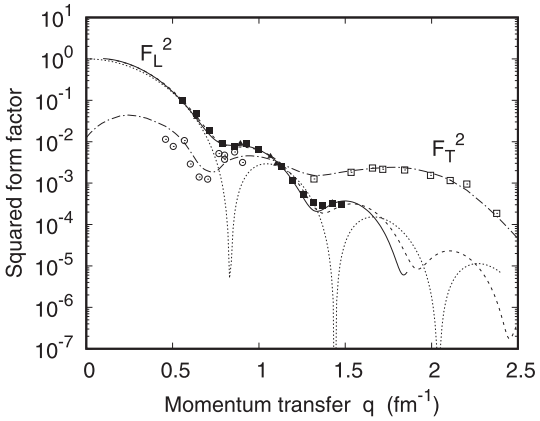

Fig. 27. Square of the electric (F_L) and magnetic (F_T) form factors for the elastic scattering of electrons from ^{115}In as a function of momentum transfer q. F_L^2 from the phase-shift analysis (————) for E_i = 183 MeV and (−−−−−) for E_i = 250 MeV, as described in the text; ·····, F_L^2 in PWBA. − ·—·—, F_T^2 taken from Donnelly and Sick [48] (plotted versus q rather than versus q_{eff}, and their F_T^2 multiplied by 4π). Included are the experimental data for F_L^2 from Crannell et al. (▲, [33]) and from Hahn et al. (■, [34]), measured in the forward hemisphere, and from Box (○, [49]) recorded at an angle near 180°. The data (□) at the higher q are taken from [48].

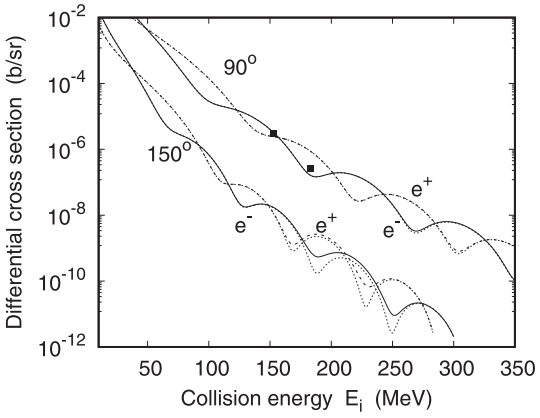

Fig. 28. Differential cross section $(\frac{d\sigma}{d\Omega})_0$ from (37) for electrons (————) and positrons (−−−−−) scattering from ^{115}In as a function of collision energy E_i. Upper curves, θ = 90°, lower curves, θ = 150°. The results (26) from potential scattering for the respective particles are also shown (·····). The experimental data for electron scattering (■) are from Hahn et al. [34].

distribution of the DCS and the Sherman function for positron scattering at some incident energies in the vicinity of the deep minimum at [E_c = 7.212 eV; θ_c = 44.6°]. It is evident from Fig. 26(c) that exactly at the critical energy (E_i = 7.212 eV), the DCS has the lowest value compared to its two adjacent values at 7.047 eV and 7.4 eV. Similarly, as shown in Fig. 26(d), the maximum values of polarization vary from +0.00224 at 44.6° to −0.0004 at 45°. However, these values of polarization are far lower than the total polarization ($S = \pm 1$).

3.3. High-energy considerations

In order to demonstrate the importance of magnetic scattering, we recall that in the plane-wave Born approximation (PWBA), the differential cross section can be represented in terms of the elastic (F_L) and magnetic (F_T) form factors [48],

$$\left(\frac{d\sigma}{d\Omega}\right)_0 = \sigma_{\text{Mott}}\left[Z^2F_L^2(q) + \left(\frac{1}{2} + \tan^2\frac{\theta}{2}\right)F_T^2(q)\right]. \tag{39}$$

Fig. 27 shows the square of $F_L(q)$ (which is normalized to unity in q = 0), obtained in the Born approximation from the Fourier-transformed charge density,

$$F_L(q) = \frac{4\pi}{Z}\int_0^\infty r^2dr\,\rho_n(r)\,\frac{\sin(qr)}{qr}, \tag{40}$$

and calculated to all orders in Z by dividing the DCS (26), obtained by means of the phase-shift analysis, by $Z^2\sigma_{\text{Mott}}$, in comparison with $F_T^2(q)$. It follows immediately from (39) that the larger the scattering angle, the more important becomes the magnetic contribution. F_T is approximately constant for $\theta \gtrsim 170°$.

The oscillatory behavior of the form factors with q (i.e. with energy, respectively angle) results from interference effects caused by the leptons scattering from the individual protons in the nucleus. These oscillations start to occur for lepton-nucleus distances, measured in terms of q^{-1}, of the order of the nuclear radius. They are the high-energy homologues of the Ramsauer-Townsend structures at low energy.

Fig. 28 displays the cross section for electron and positron impact at the two angles 90° and 150° as a function of collision energy. It is seen that at the smaller angle, magnetic scattering is unimportant, except in the cross section minima for E_i > 200 MeV. However, at 150°, it induces considerable modifications, with a strong filling of the minima from potential scattering for both lepton species. It should also be noted that electrons and positrons oscillate out of phase, the positron DCS starting to oscillate at a higher energy because of the repulsive interaction between the positron and the nucleus.

The Sherman function, calculated from (32), is depicted in Fig.29a, again for the two angles 90° and 150°. Not only are the excursions larger at 150°, the period is also reduced as compared to the results for the smaller angle. This can be explained by the $j_1(qR_N)$-behaviour of the diffraction structures. As a function of E_i, the m^{th} zero of j_1 is approximately given by $E_i = (m\pi + \lambda)c/(2R_N\sin\frac{\theta}{2})$, with $\lambda \approx 1.5$ for $3 \leqslant m \lesssim 7$, which decreases with θ. In concord with the behaviour of the cross section, the oscillations of S for positrons and electrons are not in phase, and the minima in S correspond to the minima of the DCS.

Let us now turn to the spin asymmetries U and T. In a coordinate system where the z-axis is chosen in the beam direction, while the outgoing lepton defines the (x, z)-scattering plane, U is the spin asymmetry for longitudinally (in ± z-direction) polarized beam leptons and T the one for transversely (in ± x-direction) polarized leptons. Thereby the polarization of the scattered lepton has to be fixed in transverse direction [53]. Both asymmetry parameters are, in contrast to S, non-vanishing in the Born approximation [53],

$$U^B = \frac{\sin\theta}{\sin^2\frac{\theta}{2} + \gamma^2\cos^2\frac{\theta}{2}}\left[(\gamma-1)^2\cos^2\frac{\theta}{2} + \gamma - 1\right],$$

$$T^B = \frac{1}{2(\sin^2\frac{\theta}{2} + \gamma^2\cos^2\frac{\theta}{2})}\left[(\gamma-1)^2\cos^2\theta + (\gamma^2-1)\cos\theta + 2\gamma\right], \tag{41}$$

with $\gamma = E/c^2$. In the limits $\gamma \to 1$ and $\gamma \to \infty$ they attain a simple form,

$$U^B = 0, \qquad T^B = 1, \qquad \text{for } E_i \to 0$$

$$U^B = \sin\theta, \qquad T^B = \cos\theta, \qquad \text{for } E_i \to \infty. \tag{42}$$

Fig. 29b shows the energy dependence of U for a scattering angle of

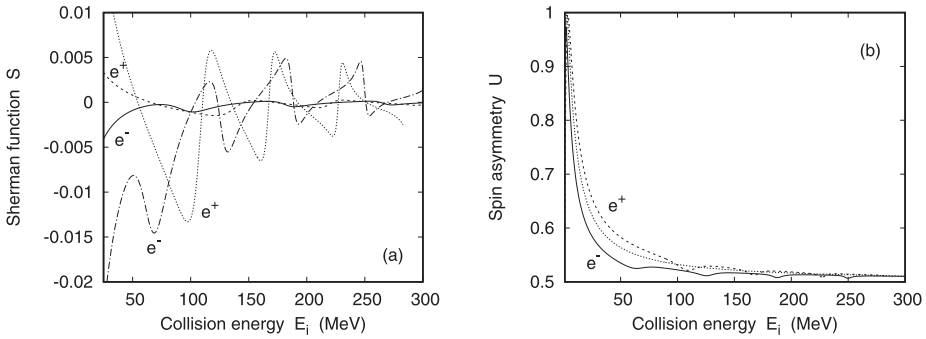

Fig. 29. Spin asymmetries for electron and positron scattering from ^{115}In as a function of collision energy E_i. (a) Sherman function for electrons (———, 90°;—·—·—, 150°) and for positrons (– – – –,90°;·····,150°). (b) Spin asymmetry U for electrons (————-) and positrons (– – – – –) at $\theta = 150°$. Included is the PWBA result U^B (·····).

150° in the Born approximation as compared to the phase-shift results for electron and positron scattering. In contrast to the diffraction structures seen for electrons or positrons, U^B decreases monotonously with E_i, tending to its high-energy limit of $\sin 150° = 0.5$. It is seen that this limit is also approached for the leptons. Moreover, as follows from 21–25, $U \approx 0$ for positrons when $E_i \lesssim 1$ keV, irrespective of θ. This indicates that for that species, also the low-energy Born limit is acquired. The same is true for T, i.e. $T \approx 1$ for $E_i \lesssim 1$ keV and $T \approx \cos\theta$ at large E_i. This small-E_i plane-wave-type behaviour of the positrons confirms our earlier result on S that the target electrons merely induce screening of the nuclear charge, and do not act as separate scattering centers.

For electron impact, on the other hand, as seen in Figs. 9–13, U and T show diffraction structures at $E_i \lesssim 1$ keV, in concord with the structures in the differential cross section.

In spin asymmetry investigations at ultrahigh energies, instead of U and T, the parameters L and R are used. These parameters are linear combinations of U and T according to

$$L = U\sin\theta + T\cos\theta, \qquad R = U\cos\theta - T\sin\theta, \tag{43}$$

with the Born limits,

$$L^B = \cos\theta, \quad R^B = -\sin\theta \quad \text{for } E_i = 0,$$

$$L^B = 1, \quad R^B = 0 \quad \text{for } E_i \to \infty. \tag{44}$$

The advantage of this change of variables is the θ-independence of the high-energy Born limits of L and R. Both parameters are, like U and T, accessible for beam electrons polarized longitudinally (for L), respectively transversely (for R). However, in that case, the outgoing lepton has to be in a helicity eigenstate (with spin polarization parallel or antiparallel to its direction of motion) [53].

4. Conclusions

The present study reports on the pure elastic and the total scattering of electrons and positrons from indium atoms over a broad energy range 1 eV$\leqslant E_i \leqslant$0.5 GeV. The calculations involving various scattering observables (DCS, ICS, MTCS, VCS, INCS, TCS) are carried out within the framework of the relativistic Dirac partial-wave phase-shift analysis. Two different theoretical approaches, OPM and NSA, are employed to cover this broad energy domain. The OPM, valid for 1 eV$\leqslant E_i \leqslant$5 MeV, considers interactions of the incident projectile with both the nucleus and the bound electrons of the target atom. Whereas the NSA, valid for $E_i \geqslant$1 MeV, incorporates only the projectile-nucleus interaction. As our target ^{115}In is a spin-9/2 isotope, the phase shift analysis is supplemented with the contributions for the magnetic scattering from the nucleus. This magnetic scattering leads to a noticeable enhancement of the differential cross section at scattering angles in the backward hemisphere and collision energies above 150 MeV. It is amazing to observe that the OPM merges smoothly with the NSA at about $1 - 5$ MeV for both electron and positron scattering.

This study provides a more detailed analysis of the CMs in the DCS distributions of both electrons and positrons scattering from indium atoms than the previous calculations. For electron-indium scattering, a total of 13 CMs are revealed and 26 maximum polarization points are obtained in their proximity, while earlier calculations predicted a smaller number of CMs. It is noted that the number of CMs depends upon the method of analysis, signifying that the analysis of CMs is highly sensitive to the method of analysis and so provides a finer test of a theory. The comparison of our elastic and total cross sections and spin asymmetries reveals an overall reasonable agreement with the available experimental data and other theoretical calculations. These results indicate that the OPM in conjunction with the NSA can provide a satisfactory description of electron-atom and positron-atom scattering over a broad energy domain. Our analysis of the CMs and the predictions for positron scattering still awaits verification by future experiments.

Credit authorship contribution statement

Sanjida Afroz: Conceptualization, Investigation. **M.M. Haque:** Writing - original draft, Visualization. **A.K. Fazlul Haque:** Supervision. **D.H. Jakubassa-Amundsen:** Software, Validation. **M.Atiqur R. Patoary:** Project administration. **M. Shorifuddoza:** Resources. **Mahmudul H. Khandker:** Resources. **M. Alfaz Uddin:** Software, Validation.

Declaration of Competing Interest

The authors declare that they have no known competing financial interests or personal relationships that could have appeared to influence the work reported in this paper.

Acknowledgment

A.K.F. Haque would like to thank TWAS-UNISCO associateship scheme for partial funding.

References

[1] Horowitz CJ. Parity violation in astrophysics. Eur Phys J A 2005;24(2):167–70. https://doi.org/10.1140/epjad/s2005-04-042-x.
[2] Hossain MI, Haque A, Patoary MAR, Uddin MA, Basak AK. Elastic scattering of electrons and positrons by atomic magnesium. Eur Phys J D 2016;70:41. https://doi.org/10.1140/epjd/e2016-60527-9.
[3] Haque AK, Haque MM, Bhattacharjee PP, Uddin MA, Patoary MA, Hossain MI, Basak AK, Mahbub MS, Maaza M, Saha BC. Relativistic calculations for spin-polarization of elastic electron-mercury scattering. J Phys Commun 2017;1(3):035014https://doi.org/10.1088/2399-6528/aa8bf8.
[4] Jakubassa-Amundsen DH. Elastic scattering of spin-polarized electrons and positrons from ^{23}Na nuclei. Nucl Phys A 2018;975:107. https://doi.org/10.1016/j.nuclphysa.2018.04.010.
[5] Haque AK, Haque MM, Hossain MS, Hossain MI, Patoary MA, Maaza M, Basak AK,

Saha BC, Uddin MA. A study of the critical minima and spin polarization in the elastic electron scattering by the lead atom. J Phys Commun 2018;2(12):125013https://doi.org/10.1088/2399-6528/aaf6bd.
[6] Khandker MH, Haque AKF, Maaza M, Uddin MA. Elastic scattering of electrons from the ions of argon isonuclear series. Phys Scr 2019;94:075402https://doi.org/10.1088/1402-4896/ab0d56.
[7] Marinković BP, Panajotović R, Šević D, McEachran RP, García G, Blanco F, Brunger MJ. Experimental and theoretical cross sections for elastic electron scattering from zinc. Phys Rev A 2019;99(6):062702https://doi.org/10.1103/PhysRevA.99.062702.
[8] Haque MM, Haque AK, Bhattacharjee PP, Uddin MA, Patoary MA, Basak AK, Maaza M, Saha BC. Relativistic treatment of scattering of electrons and positrons by mercury atoms. Mol Phys 2019;117(17):2303–19. https://doi.org/10.1080/00268976.2018.1548712.
[9] Dapor M. Polarized electron beams elastically scattered by atoms as a tool for testing fundamental predictions of quantum mechanics. Sci Rep 2018;8:5370. https://doi.org/10.1038/s41598-018-23660-4.
[10] Singh S, Naghma R, Kaur J, Antony B. Study of elastic and inelastic cross sections by positron impact on inert gases. Eur Phys J D 2018;72(4):69. https://doi.org/10.1140/epjd/e2018-80741-7.
[11] Ranković ML, Maljković JB, Tökési K, Marinković BP. Elastic electron differential cross sections for argon atom in the intermediate energy range from 40 eV to 300 eV. Eur Phys J D 2018;72(2):30. https://doi.org/10.1140/epjd/e2017-80677-4.
[12] Kumar A, Kumar S, Rastogi N, Raj D. Critical points for electron–Mg atom elastic scattering. J Phys B: At Mol Opt Phys 2018;51(3):035203https://doi.org/10.1088/1361-6455/aa9d68.
[13] McNamara K, Fursa DV, Bray I. Calculation of electron scattering on atomic silver. J Phys B: At Mol Opt Phys 2018;51(8):085203https://doi.org/10.1088/1361-6455/aab420.
[14] Sinha N, Singh S, Antony B. Positron total scattering cross-sections for alkali atoms. J Phys B: At Mol Opt Phys 2017;51(1):015204https://doi.org/10.1088/1361-6455/aa949d.
[15] Mohan H. Cross sections for electrons scattering from silver at low energies. In Journal of Physics: Conference Series 2017;875(6):052018. https://doi.org/10.1088/1742-6596/875/6/052018.
[16] Hosain ME, Patoary MA, Haque MM, Haque AF, Hossain MI, Uddin MA, Basak AK, Maaza M, Saha BC. Elastic scattering of $e^{\pm}$ by Na atoms. Mol Phys 2018;116(5–6):631. https://doi.org/10.1080/00268976.2017.1390175.
[17] Haque AK, Hossain MI, Uddin MA, Patoary MA, Basak AK, Maaza M, Saha BC. Elastic scattering of electrons and positrons by cadmium atoms. Mol Phys 2017;115(5):566. https://doi.org/10.1080/00268976.2016.1233357.
[18] Kadyrov AS, Bray I. Recent progress in the description of positron scattering from atoms using the convergent close-coupling theory. J Phys B: At Mol Opt Phys 2016;49(22):222002https://doi.org/10.1088/0953-4075/49/22/222002.
[19] Bartschat K, Tennyson J, Zatsarinny O. Quantum-mechanical calculations of cross sections for electron collisions with atoms and molecules. Plasma Process Polym 2017;14(1–2):1600093. https://doi.org/10.1002/ppap.201600093.
[20] Kariuki PK, Okumu J, Singh CS. Distorted wave Born and optical potential calculation methods for electron-sodium elastic scattering cross-section at intermediate energies. Afr Rev Phys 2015;10:0018. https://doi.org/1061-2611-1-PB.
[21] Dzhumagulova KN, Shalenov EO, Ramazanov TS. Elastic scattering of low energy electrons in partially ionized dense semiclassical plasma. Phys Plasmas 2015;22(8):082120https://doi.org/10.1063/1.4928877.
[22] Bostock CJ, Fursa DV, Bray I. Relativistic convergent close-coupling calculation of spin asymmetries for electron–indium scattering. J Phys B: At Mol Opt Phys 2012;45(18):181001https://doi.org/10.1088/0953-4075/45/18/181001.
[23] Prewitt JF, Wright LE. Elastic electron scattering and the nuclear magnetization distribution. Phys Rev C 1974;9:2033.
[24] Khandker MH, Haque AKF, Maaza M, Uddin MA. Scattering of $e^{\pm}$ from the neon isonuclear series over the energy range 1eV-0.5 GeV. Jap J Appl Phys 2020;59:SHHA05.
[25] Shorifuddoza M, Patoary MAR, Jakubassa-Amundsen DH, Haque AKF, Uddin MA. Scattering of $e^{\pm}$ from ytterbium atoms. Eur Phys J D 2019;73:164. https://doi.org/10.1140/epjd/e2019-100130-8.
[26] Haque MM, Haque AKF, Jakubassa-Amundsen DH, Patoary MAR, Basak AK, Maaza M, Saha BC, Uddin MA. $e^{\pm}$-Ar scattering in the energy range 1 eV$\leqslant Ei\leqslant$0.5 GeV. J Phys Commun 2019;3:045011https://doi.org/10.1088/2399-6528/ab16a0.
[27] Haque AKF, Uddin MA, Jakubassa-Amundsen DH, Saha BC. Comparative study of eV to GeV electrons and positrons scattering elastically from neutral atoms. J Phys B: At Mol Opt Phys 2018;51:175202https://doi.org/10.1088/1361-6455/aad6b7.
[28] Vitas N, Vince I, Lugaro M, Andriyenko O, Gošić M, Rutten RJ. On the solar abundance of indium. Mon Not R Astron Soc 2008;384(1):370–5. https://doi.org/10.1111/j.1365-2966.2007.12708.x.
[29] Djeniže S, Srećković A, Bukvić S. The first measurement of the In III Stark widths. Spectrochim Acta, Part B 2006;61(5):588–91. https://doi.org/10.1016/j.sab.2006.04.003.
[30] Becker T, Zanthier JV, Nevsky AY, Schwedes C, Skvortsov MN, Walther H, Peik E. High-resolution spectroscopy of a single In^{+} ion: progress towards an optical frequency standard. Phys Rev A 2001;63(5):051802https://doi.org/10.1103/PhysRevA.63.051802.
[31] Rabasović MS, Kelemen VI, Tošić SD, Šević D, Dovhanych MM, Pejčev V, Filipović DM, Remeta E Yu, Marinković BP. Experimental and theoretical study of the elastic-electron-indium-atom scattering in the intermediate energy range. Phys Rev A 2008;77(6):062713. https://doi.org/10.1103/PhysRevA.77.062713.
[32] Bartsch M, Geesmann H, Hanne GF, Kessler J. Asymmetric scattering of polarized electrons from atoms with closed and open shells. J Phys B At Mol Opt Phys 1992;25(7):1511. https://doi.org/10.1088/0953-4075/25/7/021.
[33] Crannell H, Helm R, Kendall H, Oeser J, Yearian M. Scattering of high-energy electrons from Ca^{40}, V^{51}, Co^{59}, In^{115}, $Sb^{121,123}$ and Bi^{209}. Phys Rev 1961;121(1):283. https://doi.org/10.1103/PhysRev.121.283.
[34] Hahn B, Ravenhall DG, Hofstadter R. High-energy electron scattering and the charge distributions of selected nuclei. Phys Rev 1956;101(3):1131. https://doi.org/10.1103/PhysRev.101.1131.
[35] Öztürk N, Williamson Jr W, Antolak AJ. Elastic scattering of electrons and positrons by bound phosphorus, indium, and antimony atoms. J Appl Phys 1992;71(1):11–5. https://doi.org/10.1063/1.350741.
[36] Dapor M, Miotello A. Differential, total, and transport cross sections for elastic scattering of low energy positrons by neutral atoms (Z= 1–92, E= 500–4000 eV). At Data Nucl Data Tables 1998;69(1):1. https://doi.org/10.1006/adnd.1998.0771.
[37] Bartschat K. Mott scattering and angular momentum orientation low-energy electron scattering from indium atom. J Phys B At Mol Opt Phys 1992;25(12):L307. https://doi.org/10.1088/0953-4075/25/12/006.
[38] Mayol R, Salvat F. Total and transport cross sections for elastic scattering of electrons by atoms. At Data Nucl Data Tables 1997;65(1):55–154. https://doi.org/10.1006/adnd.1997.0734.
[39] Salvat F, Fernández-Varea JM, Williamson Jr W. Accurate numerical solution of the radial Schrödinger and Dirac wave equations. Comput Phys Commun 1995;90(1):151–68. https://doi.org/10.1016/0010-4655(95)00039-I.
[40] Salvat F, Jablonski A, Powell CJ. ELSEPA-Dirac partial-wave calculation of elastic scattering of electrons and positrons by atoms, positive ions and molecules. Comput Phys Commun 2005;165(2):157–90. https://doi.org/10.1016/j.cpc.2004.09.006.
[41] Koga T. Analytical Hartree-Fock electron densities for atoms He through Lr. Theor Chim Acta 1997;95(3–4):113–30. https://doi.org/10.1007/BF02341696.
[42] Furness JB, McCarthy IE. Semiphenomenological optical model for electron scattering on atoms. J Phys B: At Mol Phys 1973;6(11):2280. https://doi.org/10.1088/0022-3700/6/11/021.
[43] Jain A. Low-energy positron-argon collisions by using parameter-free positron correlation polarization potentials. Phys Rev A 1990;41(5):2437. https://doi.org/10.1103/PhysRevA.41.2437.
[44] http://physics.nist.gov/PhysRefData/ASD/levels_form.html.
[45] Smirnov BM, Radtsig AA. Reference Data on Atoms, Molecules, and Ions. Berlin: Springer-Verlag; 1985.
[46] Yennie DR, Ravenhall DG, Wilson RN. Phase-shift calculation of high-energy electron scattering. Phys Rev 1954;95(2):500. https://doi.org/10.1103/PhysRev.95.500.
[47] Jakubassa-Amundsen DH, Barday R. The Sherman function in highly relativistic elastic electron-atom scattering. J Phys G 2012;39:025102.
[48] Donnelly TW, Sick I. Elastic magnetic electron scattering from nuclei. Rev Mod Phys 1984;56(3):461. https://doi.org/10.1103/RevModPhys.56.461.
[49] Box G. [Ph.D. thesis]; 1976.
[50] Lucas MW, Jakubassa-Amundsen DH, Kuzel M, Groeneveld KO. Quasifree electron scattering in atomic collisions: the Ramsauer-Townsend effect revisited. Int J Mod Phys A 1997;12:305–78.
[51] Überall H. Electron Scattering from Complex Nuclei. New York: Academic; 1971.
[52] Walker DW. Relativistic effects in low energy electron scattering from atoms. Adv Phys 1971;20(85):257–323. https://doi.org/10.1080/00018737100101251.
[53] Motz JW, Olsen H, Koch HW. Electron scattering without atomic or nuclear excitation. Rev Mod Phys 1964;36(4):881. https://doi.org/10.1103/RevModPhys.36.881.